SURFACE DIRECTED ELECTROKINETIC FLOWS IN MICROFLUIDIC DEVICES

by

MEHMET BASAR KARACOR

A thesis submitted to the

Graduate School-New Brunswick

Rutgers, The State University of New Jersey

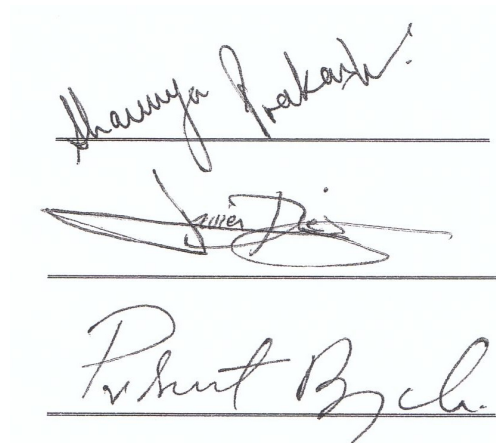in partial fulfillment of the requirements

for the degree of

Master of Science

Graduate Program in Mechanical and Aerospace Engineering

written under the direction of

Dr. Shaurya Prakash

and approved by

_____

_____

_____

New Brunswick, New Jersey

October, 2009

ABSTRACT OF THE THESIS

Surface Directed Electrokinetic Flows in Microfluidic Devices

By MEHMET BASAR KARACOR

Thesis Director:

Dr. Shaurya Prakash

Electroosmotic flow control in microfluidic devices is an important and challenging problem, as electroosmosis directly influences separation efficiencies in lab-on-chip applications. In this study, a non-mechanical passive flow directing method is presented for electrokinetically driven flow. Due to the high surface-area-to-volume (*SA/V*) ratio, surface properties dominate the flow in microfluidic channels. For electrokinetically driven flows, the main surface property affecting electroosmotic flows is the surface ζ potential, which is related to the effective surface charge density. By changing the effective surface charge density, the electroosmotic flow rates of charged species can be controlled in microfluidic channels. In this work, to change the effective surface charge density, surfaces were chemically modified with $-Br$, $-NH_2$ and $-CH_3$ functional groups by 'click' chemistry. Since these functional surface layers are integrated within model glass microfluidic devices prepared by standard microfabrication procedures, the first step was to investigate the stability of the adherent surface layers to a variety of microfabrication conditions. A model "Y" shaped glass microfluidic device was developed. One leg of this model microfluidic device was selectively chemically

modified to alter the ζ potential and thereby increase or decrease the electroosmotic flow with respect to rest of the device. Electroosmotic flow is visualized by using marker dyes under a fluorescent microscope. In addition, experiments were validated by using the CFD code in COMSOL. The experiments concluded that the surface layers are stable to a variety of conditions including a wide pH range (pH 3 – pH 11), solvent exposure, acid and base exposure, and UV light. Extreme conditions such as a piranha solution or oxidative plasma degrade the surface layers. Electrokinetic flow experiments show that depending on the charge of a species the electroosmotic flow is preferentially directed as a function of the ζ potential in the microfluidic channels.

Acknowledgement

First of all I would like to thank to my each family member one by one whose everlasting support made this work possible. And, I would like to specially thank to my best friend since the age of 8, Ates Civitci, for his great support from the time I arrived to Rutgers University till now and also for his patience and help to my never ending demands. I would also like to thank to Efruz Hatipoglu, Eyup Akdemir, Marita Torregrosa, and Berrak Canova for their close and strong friendship. Also, I would like to thank to my classmates, and friends for their friendship.

I would like to specially thank to Dr. Shaurya Prakash for his mentoring, advices, support, and guidance since the beginning of my graduate level education.

Table of Contents

List of Tables

List of Illustrations

Chapter 1

Introduction

1. Microfluidics

Microfluidics deals with fluid flows at device length scales in the range of 10-100 μm critical dimension [1]. However, with the advent of nanofluidics, which commonly deals with 1-100 nm length scales [2], the definition of microfluidics was expanded to include the length scales between 100 nm and 100 μm. One of the early motivations behind the development of microfluidics started with the aim of miniaturizing room and bench-top size laboratory systems and tools such as clinical diagnostic systems, biomedical devices, electrophoretic separation systems, chemical and biochemical analyses tools [1, 3]. The earliest reported microfluidic device was fabricated on silicon wafers with conventional microfabrication techniques such as photolithography and wet etching by Terry *et al.* [4] for gas chromatography applications. The earliest reported liquid-based microfluidic device was first fabricated for liquid chromatography applications, also on a silicon chip [5]. Another early application in microfluidics was the ink jet printing nozzles developed by IBM [6, 7]. There are many advantages with the development of microfluidics that open new research and motivation areas for the further development of microfluidics.

One of the advantages of miniaturizing the systems discussed above is that the amounts of samples and reagents used, especially for medical and biology related applications, can be reduced significantly. The minimal use of reagents is beneficial as in some applications reagents and materials can be extremely expensive (several hundred dollars for a few mg) or be available in minute quantities. In addition, the reaction,

analysis, and throughput time scales can be improved with increasing the efficiency of the process and portability of the systems [3]. Smaller systems also permit much easier portability allowing for the development of portable sensors for chemical and biochemical threats for security applications [8]. The advantages gained through the developments in microfluidics also led to rapid growth in genomics research [8]. In order to further enhance the utility of microfluidics and develop the next generation devices and systems, microfluidic devices need precise fluid handling to perform processes. In a microfluidic devices fluid handling is done by microfluidic components such as micropumps, microvalves and micromixers. However, the working principles of microfluidic components depend on the driving method for the flow in a microfluidic system. There are two main driving methods pressure and electrokinetics for driving flow at these length scales.

1.2. Pressure Driven Flows

Pressure driven flow is the flow under an applied pressure gradient across the microfluidic channel. Many types of micropumps are used to apply the pressure gradient across the microfluidic channels in a device. One of the first micropumps was fabricated to produce steady state flow of dilute gas mixtures for micro analytical synthesis application as a 8 cm^3 plunger pump [9]. Early fluidic silicon micropumps were fabricated as a membrane based diaphragm pumps [10]. Later microfluidic pumps were categorized as mechanical and non-mechanical micropumps [11]. Non-mechanical pumps have no moving parts and achieve pumping by other mechanisms such as ac magnetohydrodynamic pumping[12], pumping with controlling bubble formation in microfluidic channels, [13] and

pumping magnetically ferrofluid plugs in microfluidic channels [14]. However, a need arises with the control of fluid flow in the device. Microvalves are used to fulfill the need.

The first microvalve, which was actuated by a magnetic field, consisted of a nickel diaphragm actuated with a plunger solenoid. The first report of the microfabricated valve is dated by to the work of Terry *et al.* [4]. Microvalves can be also categorized as mechanical and non-mechanical microvalves. There are different types of actuation mechanisms for mechanical microvalves such as external magnetic field [15, 16], piezoelectric [17, 18], thermopneumatic [19, 20], shape memory alloys [19, 21], membrane [22, 23] and for non-mechanical microvalves such as electrochemistry [24], phase change [19, 25-27], and relative hydrophobicity [28-30].

Pressure driven flows can be a challenge with shrinking length scales. The required pressure gradient for a given flow rate in capillaries is related to the fourth order of diameter of the capillary according to the Hagan-Poisuille equation.

$$Q = \frac{\pi R^4 \Delta P}{8 \mu L} \tag{1}$$

Q is the volumetric flow rate, R is the radius of the capillary, L is the length of the capillary. Due to the required pressure gradient to drive the fluid in a capillary, powerful external systems is required. The required pressure difference for 1 ml/s flow rate in 3 cm length channel with various channel diameters is presented in Table 1.1

Table 1.1: Required pressure difference for 1 ml/s flow rate in 3 cm channel with various diameters

Channel Diameter (μm)	Required Pressure Difference (MPa)
100	1.22×10^{-2}
10	1.22×10^{2}
1	1.22×10^{6}
0.1	1.22×10^{10}

1.3 Electric Double Layer Structure and Zeta Potential

Before going in to the electrokinetic flows, electric double layer and zeta potential should be addressed. Electric double layer (EDL) is an electrical structure that, forms on a charged surface when the surface is in a contact with an electrolyte solution, with different sub-layers in it which is presented in Figure 1.1.
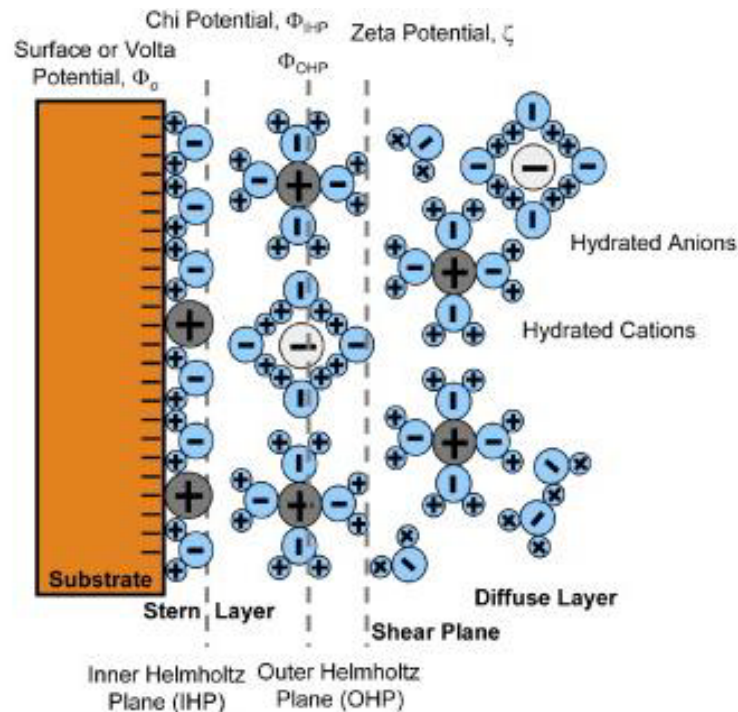
Figure 1.1 Electric double layer structure [31]

The first layer is the Stern Layer which shields the surface charge ions with counter ions in the electrolyte solution. Due to the shielding layer, ions are attracted to the shielding layer which forms another sub-layer consist of ions in the electrolyte solution. The electrical potential of this layer is defined as ζ potential of the surface. The outer layer is the diffuse layer, which neutralizes the ζ potential along the electrolyte solution. At the end of the diffuse layer which is the bulk of the electrolyte solution is neutral. The surface ζ potential is related to the measurable quantity, surface charge density by the modified Grahame equation:

$$\sigma_s = \frac{2\varepsilon\varepsilon_0 kT}{\lambda_D e}\left[\sinh\left(\frac{e\zeta}{2kT}\right) + \frac{2\lambda_D}{a}\tanh\left(\frac{e\zeta}{4kT}\right)\right]$$
(2)

where, a is the pore diameter, λ_D is the Debye length, and e is the elementary charge. A commonly used expression for computing λ_D is given by equation:

$$\lambda_D = \frac{1}{\kappa} = \sqrt{\frac{\varepsilon\varepsilon_0 RT}{2F^2\sum_i c_i z_i^2 / 2}}$$
(3)

where, F is the Faraday constant, c is the concentration of species i, and z the ionic valence of species i.

1.4 Electrokinetic Phenomena

Electrokinetic flow is the fluid flow under an electric field. But, specifically the transport of the liquid media caused by the movement of ions under an electric field is called electromigration in microfluidics. There are three different electrokinetically driven flow types in microfluidics [3] such as electrophoresis, conduction current caused by streaming potential, and electroosmotic flow [3].

Electrophoresis is the particle movement under an electric field which is applied to the bulk liquid. Since every different type of particle has different charge on their

surface or mobility in a liquid, electrophoresis of a particle is used to separate some of them from other types of particles. The other electrokinetic flow is the conduction current which is derived with a pressure gradient across the channel.

When a pressure gradient is applied to an electrolyte solution in a microfluidic channel, counter-ions on the charged surface starts moving in the applied pressure direction inducing a current and an electrical potential between the outlet and the inlet[3]. This potential is called streaming potential[3]. There is also an ion flow under the streaming potential direction which causes a current opposite to the direction of streaming current and is called the conduction current.

The last electrokinetic flow is the electroosmotic flow which also starts with the flow of counter ions on the charged surface of channels. If an electric field is applied to a microchannel filled with an electrolyte solution, the counter-ions start moving in the diffuse layer of electric double layer (EDL). Moving counter-ions drags fluid around them which causes a bulk flow which is called electroosmotic flow (EOF) and was first introduced by Reuss [32] in 1809 [3]. In order to transport liquids in lab-on-chip devices electroosmotic flow is commonly used by applying electric field across the device[3].

Since EOF is used for in a microfluidic device, EOF of a substance can be controlled to solve the fluid handling needs in a microfluidic device by controlling the counter-ion movement, which in-turn depends on the applied field and the surface properties [3]. Therefore, surfaces can also be used for flow manipulation by controlling surface properties in a microfluidic device due to the high area-to-volume (*SA/V*) for microchannels with SA/V ratios as high as 10^9 m^{-1} being reported.

1.4 Surface Controlled Microfluidic Flows

A common application of surface controlled microfluidic flows is mixing in heterogeneous surfaces. Use of surface heterogeneity within the microfluidic devices through systematically patterned regions of surface charge or non-uniform zeta, ζ potentials has been shown to assist in mixing phenomena [33, 34]. ζ potentials are defined as the potential at the slip-plane near a charged surface in contact with an electrolyte solution. Heterogeneous surfaces in microfluidic channels cause local circulation regions due to the varying electroosmotic flow rates arising on account of differences in local ζ potentials [34, 35]. These circulation regions subsequently enhance the mixing of analytes in the microchannel. Recently, an investigation of the 3D vortex generation was studied by micro-particle image velocimetry (PIV) [36]. The 3D vortex is generated with step changes of surface ζ potential by chemical surface modification of surface [36]. It is reported that it is possible to generate vortices in EOF with change of surface ζ potential with same charge polarity [36]. This is an interesting discovery since vortex generation in microfluidics can be a serious challenge as most flows are in the Stokes regime with Reynolds numbers well below 10. In addition, the direction of the electroosmotic flow depends on the surface ζ potential charge polarity of the region.

Electroosmotic velocity is related to the electroosmotic mobility of the fluid and applied electric field. The electroosmotic mobility is related to the surface ζ potential according to the Helmholtz-Smoluchowski equation where η is the viscosity and ε is the relative permittivity of the medium.

$$\mu_{EOF} = \frac{\varepsilon\zeta}{\eta} \tag{4}$$

And, the electroosmotic velocity is

$$\vec{u}_{EOF} = \mu_{EOF}\,\vec{E} \tag{5}$$

So, the electroosmotic velocity direction depends on the surface ζ potential polarity for an applied electric field.

The change in the EOF velocity profile due to a step change in surface ζ potential was studied by Herr *et al.*[37]. The step change in ζ potential shows a supporting or suppressing effect on the EOF and depends on the direction of the field[37] which is presented in the Figure 1.1.
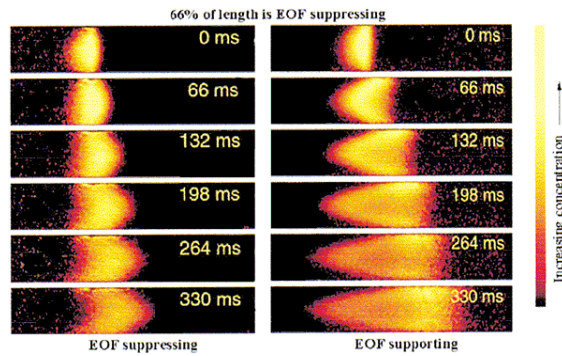
Figure 1.2: The velocity profile change due to a step change in surface ζ potential is presented. Depending on the direction of the applied field the step change in ζ potential serves as supporting or suppressing the EOF [37]

Prakash *et al.*[38] also showed that the direction of the flow depends on the surface ζ potential charge polarity. The surface ζ potential is altered by surface modification in a glass microfluidic device to show the direction change of EOF with the change of ζ potential charge polarity under same direction of applied field[38]. Recently EOF rate changes due to the dynamic adsorption of protein molecules on the surface was observed[39]. It has been shown that it is possible to manipulate the EOF with controlling surface properties, particularly surface ζ potential, to manipulate the EOF in microchannels.

In order to change the EOF in a microfluidic channel surface properties, particularly surface ζ potential must be changed. There are different ways to change the properties of a microfluidic channel surface such as plasma activation [40], in channel polymeric patches [41], and chemical modification [31, 38]. The chemical modification gives different opportunities of surface adhered chemical groups thereby providing a variety of chemical terminations and a wide range of surface ζ potentials. This gives an opportunity to engineer the microfluidic surfaces as needed. One of the methods to chemically modifying in micro- nanofluidic channels is functionalizing silica surfaces with silicon based self assembled monolayers (SAM) [38, 42-45] as described next.

1.6 Self Assembled Monolayers

Generally a self-assembled monolayer (SAM) has 3 parts, the head-group, backbone, and an end-group as illustrated in Figure 1.2 [46] The head-group links to the surface and makes linkages between adjacent molecules to form a network on the surface. The backbone is typically a hydrocarbon chain that connects the head-group to the end-group. End-group is the functional group of the SAM that interacts with the environment.
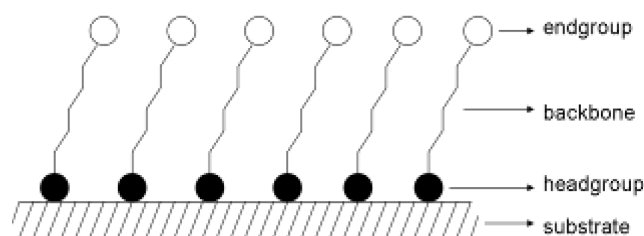
Figure 1.3: Illustration of SAM [46]

For the silane based SAMs the head group is $-SiCl_3$ or $-SiCl$. The head group reacts with the surface $-OH$ groups and thin water film on the surface of the substrate. This elimination reaction forms HCl leading to the formation of a Si-O bond with the surface and a cross-linked network with Si-O-Si bond with other SAM molecules. The backbone

is a hydrocarbon chain with a structure of $(-CH_2)_n$. End group changes the surface properties, since it is this part of the SAM that most commonly is in direct contact with the external environment. End groups can have a lot of different functional groups such as $-COCH_3$[47], $-CN$[47], and $-Br$[47] which gives the different characteristics of the surfaces such as surface charge density, wettability or reactivity. There are different methods to deposit SAMs on a surface. The most common methods are solution deposition[48-54] and gas phase deposition methods[55] for the formation of SAMs[46]. However, the exact growth mechanism of silane-based SAMs is a continuing source of scientific debate. There are three possible types for the formations of SAMs on a substrate. These are "Island Growth", "Uniform Growth", and "Random Growth" type[56].

1.5.1 Island Growth

In island growth type SAM molecules are deposited on the surface forming gathered groups on the surface called islands[56]. New SAM molecules deposited at the edge of islands with bonding to the island continuously to form a complete layer on the surface[56]. The illustration of the island growth is presented in Figure 1.3[56].
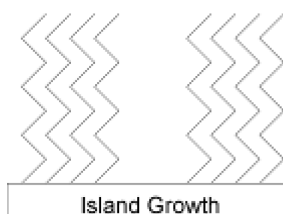
Island Growth

Figure 1.4: The illustration of island growth of SAMs[56]

1.5.2 Uniform Growth

Uniform growth type describes the SAM growth as the molecules lay down on the surface and in time molecules start packing together and extending out their backbones[49].

Figure 1.5: The illustration of uniform growth of SAMs [56]

1.5.3 Random Growth

Random growth type describes the growth as the molecules land on the surface on a random location covalently linking to the surface [56] which is illustrated on Figure 1.5.
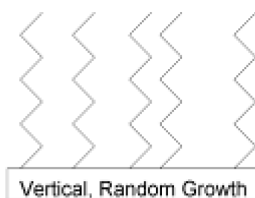
Figure 1.6: The illustration of random growth of SAMs [56]

There are many factors that effects the growth of silane-based SAMs such as relative humidity [50, 52, 53] of the surroundings in which the deposition is being carried out, the water content of solution, substrate [57-59] type, concentration of absorbent solution, temperature of the solution [52], age of solution, and solvents.

1.6. Formation Factors For SAMs

To achieve the formation of silane-based SAMs, low humidity atmosphere (nitrogen [49, 52, 53], dry [50] atmosphere) has been used in many studies. It has been observed that when alkyltrichlorosilane, which is binding to surface, is exposed to water, a visible film, which is not possible to wipe out, is formed on the surface [53]. But, it is also shown that water is involved in the formation of silane based SAMs. Si-O-Si bonds between alkylsilane part of monolayer and SiOH bonds between alkylsilane in the solution and hydroxyl groups on the surface are formed with the existence of water [50, 52, 53]. Therefore, it appears that while some water maybe necessary for the surface reactions to occur the

exact mechanism and amount of water required are not known *a priori* and are often determined through an iterative experimental procedure.

While, SAMs are an interesting area of research, there is an additional advantage to using SAMs. These surface adhered monolayers can be used to attach other molecules to surfaces for building of complex surface functionalities via synthetic chemistry procedures such as 'click' chemistry [38, 60].

1.7. "Click" Chemistry Modification

Silicon based SAMs on glass substrates are used for changing functional groups on the surface by "click" chemistry to manipulate flow in microfluidic channels [61]. During one of the "click" chemistry step, which is azide replacement, azide degradation due to the substrate effect is shown for glass and silicon substrates [62] in Figures 1.6 and Figure 1.7.
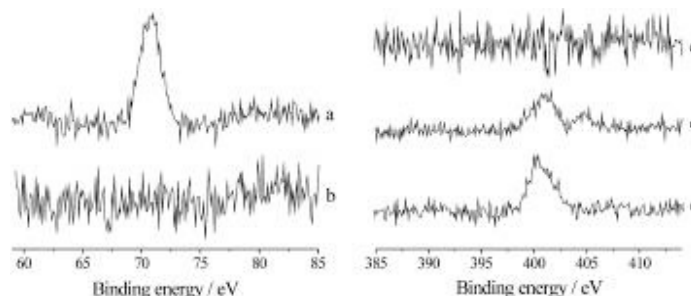
Figure 1.7: XPS spectra for Si substrate Left: Br(3d) region **a)** bromine terminated substrate **b)** azide terminated substrate Right: N(1s) region **c)** bromine terminated substrate **d)** azide terminated substrate **e)** click terminated substrate [31, 62]

The XPS spectra of Si substrate subject to the surface modification are shown in Figure 1.6. After the azide replacement the N(1s) double peak is observed for the Si substrate but not for glass substrate which is presented in Figure 1.7[62]. The bare glass substrate XPS spectra shows an additional peak at 64 eV which is the Al additive in the glass substrate [62].
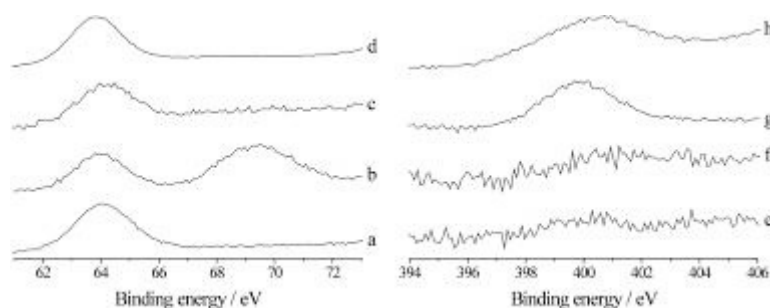
Figure 1.8: XPS Spectra for glass substrate Left: Br(3d) region **a)** bare substrate **b)** bromine terminated substrate **c)** azide terminated substrate **d)** click terminated substrate Right: N(1s) region **e)** bare substrate **f)** bromine terminated substrate **g)** azide terminated substrate **h)** click terminated substrate [31, 62]

In this thesis, electroosmotic flow directing with the modification of ζ potential due to chemical surface modification methods by deposition of $-Br$, $-NH_2$, $-CH_3$ groups through SAM or 'click' chemistry within glass microfluidic devices is described. During fabrication of microfluidic devices, surfaces undergo a variety of processing conditions with different solvents, thermal cycling, pH, UV light exposure, plasma exposure, and other chemical exposures. Also, during the characterization of microfluidic devices, surface adhered layers undergo different working conditions such as working fluids at different pH values, solvents, local temperature gradients arising out of joule heating, exposure to salt solutions and analytes, and other chemicals. Therefore, it is vitally important to ensure that the surface layers are stable under both the microfabrication and operation conditions. The stability of surface coatings created on flat surfaces, selective surface modification of microfluidic channels, and electroosmotic flow experiments to show electroosmotic flow directing was also investigated and is described in this work.

Chapter 2

Methods and Experiments

2.1. Introduction

This chapter describes the materials and methods that are used to fabricate the model "Y" shaped glass microfluidic device, selectively surface modification of the microfluidic channels, materials that used in processes, characterization and experimental methods.

2.2. Fabrication of model "Y" shaped Microfluidic Device

Glass microfluidic device fabrication is done by microfabrication methods such as piranha cleaning, metal layer deposition, photolithography, wet etching and Ca assisted glass bonding. To fabricate the glass microfluidic device cover glass slides (Fisher Scientific, 12-540C) as device layer, microscope slides (Fisher Scientific, 12-550A) as cover part are used. The microfabrication of the patterned part of the device is performed in class 1000 cleanroom (Micro Electronics Research Lab-MERL) facility.

The cleaning procedure is done before the metal deposition step to have uniform metal deposition. The piranha cleaning is a surface cleaning method that cleans the organic compounds on the surface. H_2SO_4 (Sulfuric Acid) and H_2O_2 (Hydrogen Peroxide) is mixed to form atomic O (Oxygen) as in the reaction below.

$$H_2SO_4 + H_2O_2 \rightarrow H_3O^+ + HSO_4^- + O \qquad (6)$$

The atomic O bonds with C (Carbon) in hydrocarbon chains of organic compounds on the surface of glass and forms CO_2 (Carbon dioxide) and OH on the surface as illustrated at the Figure 2.1. After the hydrocarbon chain is broken by atomic Oxygen the organic compounds are cleaned away from the glass surface due to the oxidation. The procedure

for piranha cleaning followed during device development and fabrication can be found in Appendix 1.

The aim of the metal deposition is to create a protective layer for the unpatterned regions that will not be etched to form the microchannels during device fabrication. The wet etching was done with HF (Hydrofluoric Acid) to form the microfluidic channels on the glass slide. The clean glass slides were placed in a metal evaporator (Ferrotec-Inficon IC 6000) and 50 nm thick Cr (Chromium) layer was deposited followed by a 100 nm Au (Gold) layer with E-beam evaporation under ultra high vacuum (10^{-6} Torr). The metal deposition process is illustrated below in Figure 2.1.

Photolithography process is a process that helps to define features for formation and fabrication of channels and other architectures on the substrate materials. The process consists of spin coating a substrate with a photo-active polymer, called a photoresist and exposing the photoresist coated substrate under a photomask to a UV light source at 140 mJ/cm^2 to transfer the pattern to the substrate. A schematic for the photomask used in this work can be seen in Appendix 3. Since, the photoresist used in this work is a positive-tone resist, the exposed part of the photoresist on the substrate is cross-linked and becomes reactive with the developer to remove the exposed regions and transfer the pattern to the substrate for further etching.

During this process AZ1518 as a photoresist, AZ 400K as a developer is used. The mask aligner (Karl Suzz) is used for the alignment of the photomask and substrate which is coated with photoresist. The type of the photomask aligner is a contact mode aligner which means that the substrate and the mask are in contact during the exposure to UV light. At the end of the photolithography process the patterned surface is examined

with a conventional light microscope. If defects on the patterned surface are observed, whole process is repeated. The schematic of the procedure and detailed procedure is presented below.

The Au and Cr layers are etched through by Au etchant (Transene, Gold Etchant TFA) and Cr etchant (Transene, Chromium Mask Etchant). After each metal layer is etched through, the substrate is checked under conventional light microscope for any defects. The schematic of the procedure and detailed procedure is presented below.

Microfluidic channels are etched through with diluted HF (4:1 DI water:HF). The etch rate of the HF is dependent to the type of glass and concentration of the solution. The channels are etched through for 10 min. After the glass etching, the photoresist and metal layers are stripped off. The channel depth is checked with Profilometer (Dektak) as 9.8 µm. The schematic of the procedure and detailed procedure is presented below.

To cover the patterned slide, microscope slides are used. First, for fluidic connections microscope slides are drilled with 2 mm diameter diamond drill at 1800 rpm at the reservoir points. During bonding the holes are aligned to the reservoirs on the patterned slide. Before the bonding process the patterned slides are freshly cleaned with piranha cleaning procedure.

Ca assisted bonding [63] is used to bond patterned glass slide and the cover slide. Ca assisted glass bonding is developed by Allen *et. al.* [63]. Glass slides are cleaned by wiping the surface with 1% (w/v) Alconox solution following with rinsing slides with 0.5 % (w/v) Alconox 0.5% (w/v) Calcium(II) Acetate Hydrate solution [63]. After rinsing the slides with DI water, some of the DI water is trapped between slides [63]. The slides are fixed with paper clips and baked at 60 ºC for an hour and 115 ºC for two hours [63].
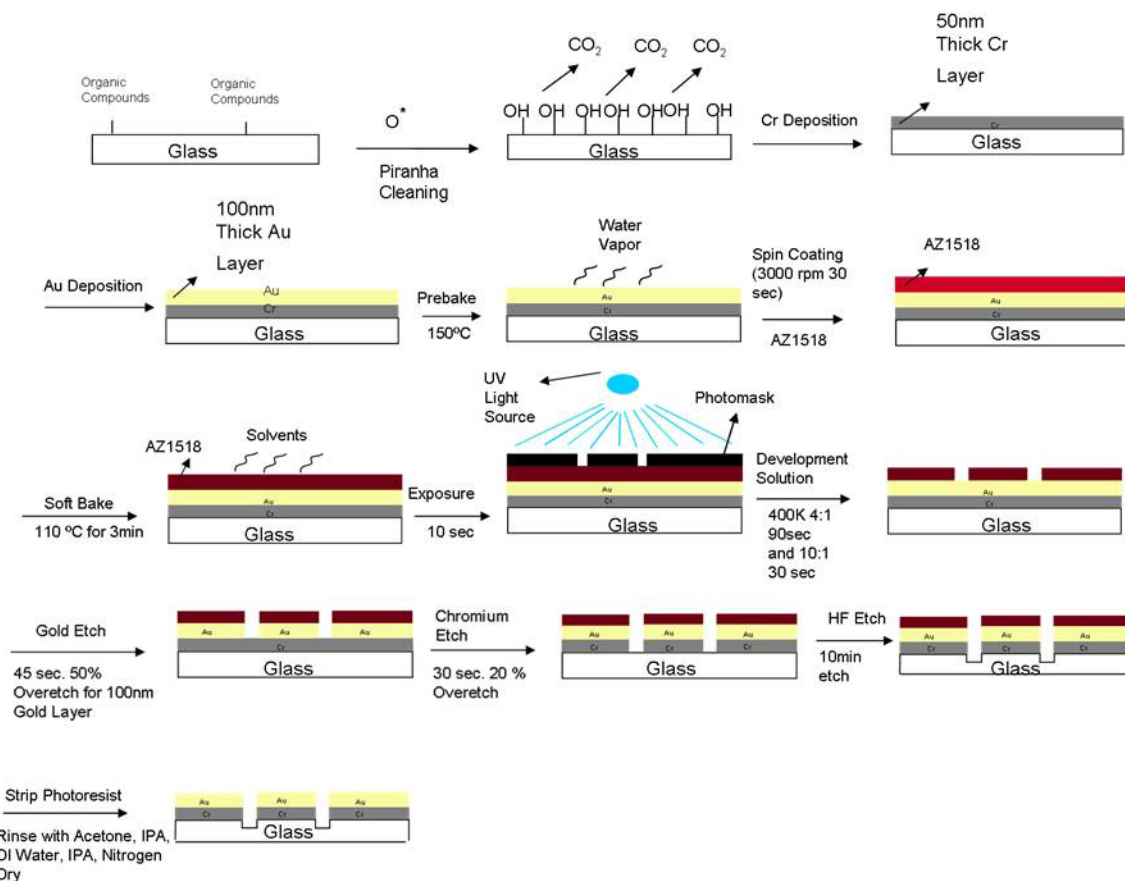
Figure 2.1: The schematic illustration of the microfabrication process of model microfluidic device

2.3. Functionalization of Flat Surfaces

As discussed in Chapter 1, one of the methods to chemically modify silica surfaces contained within microfluidic channels is functionalizing silica surfaces with silane-based self assembled monolayers (SAMs) [38, 42-45]. While, SAMs are an interesting area of research, there is an additional advantage to using SAMs. These surface adhered monolayers can be used to attach other molecules to surfaces for building of complex surface functionalities via synthetic chemistry procedures such as 'click' chemistry [38, 60]. In the process (see Appendix 7) reported in this work, a modular approach to surface modification is used [38, 60] and is shown in Figure 2.2.
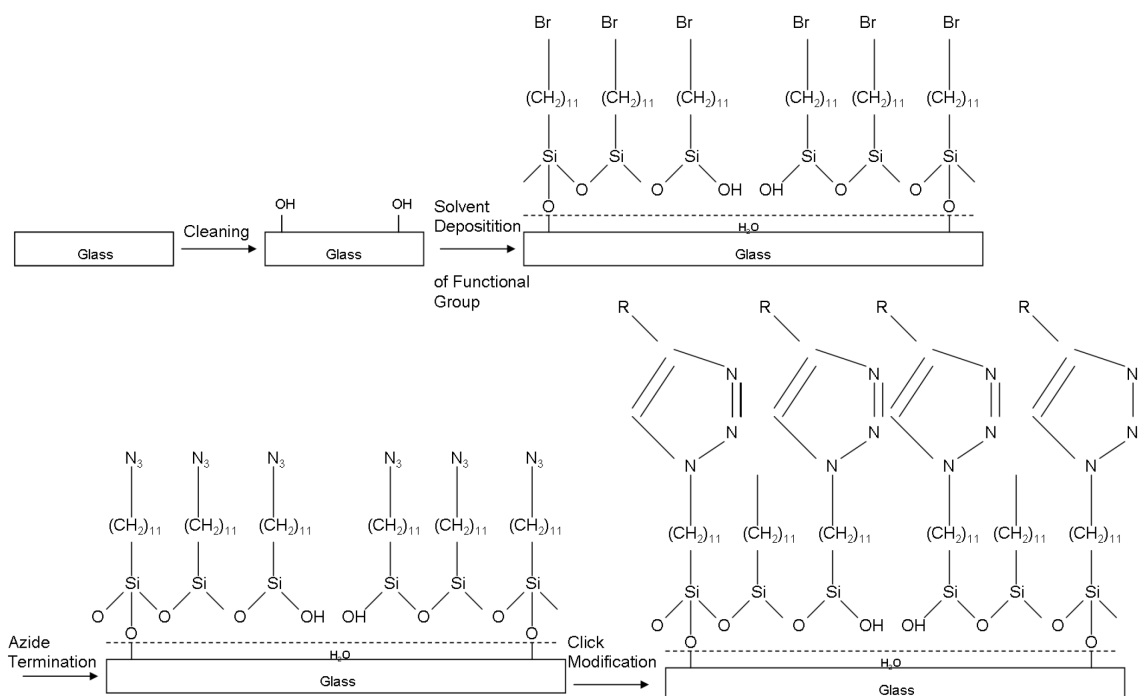
Figure 2.2: Illustration of chemical surface modification of flat glass surfaces, R is the functional groups such as $-NH_2$, $-CH_3$

As seen from Figure 2.2, the first step requires formation of a $-Br$ terminated SAM. For the self assembly of Br, 11-bromoundecyltrichorosilane (BUTS; Gelest, Inc., Morrisville, PA) was deposited as the starting surface layer from the solution phase from 1% v/v anhydrous cyclohexane (Sigma-Aldrich, MO) with a 2-hour soak time. Given the sensitivity of most silanes to water, the procedure was carried out under dry nitrogen at low relative humidity level (RH < 5%). Next, samples are soaked in to anhydrous cyclohexane and N, N-dimethylformamide (DMF) (Sigma-Aldrich, Saint Louis, MO) to remove the physisorbed BUTS from the surface.

Surfaces with bromo groups are immersed in a saturated solution of sodium azide (Acros Organics, Fair Lawn, NJ) in DMF for 48-hours to perform the S_N2 nucleophilic substitution replacement with the surface bromo groups. The samples were rinsed with DMF and dried under a dry nitrogen stream. It should be noted that sodium azide is an extremely dangerous chemical. Proper safety precautions should be taken before handling

sodium azide. Azide-terminated substrates were soaked for 2 hours in the 'click' solutions in the presence of a copper-based catalyst to perform the Huisgen cycloaddition reaction. The 'click' solution was a 10 mM propargyl amine (Sigma-Aldrich, Saint Louis, MO) solution for $-NH_2$, 10 mM 1-octyne (Sigma-Aldrich, Saint Louis, MO) solution for $-CH_3$ formation on the surfaces. The solvent in the 'click' step is ethanol (Sigma-Aldrich, Saint Louis, MO). Finally, the substrates were soaked in a 1% v/v aqueous ammonia solution to remove any surface-trapped Cu catalyst and rinsed with DI water before drying in a stream of dry nitrogen.

2.4. Functionalization of Microfluidic Channel Surfaces in Microfluidic Device

For the functionalization of microfluidic channels, the procedures for flat surfaces were followed in terms of the time-scales and control of relative humidity. However, some procedural changes are required as only the channel surfaces are modified in this work. Therefore, auxiliary equipment is required to fill-in the channels with the appropriate solutions. All channels were filled with either solvents, cleaning solutions or functionalization solutions, a vacuum pump is connected to the outlet of the microfluidic channels by using a vacuum pump to drive fluid selectively in microfluidic channels by creating a pressure gradient. In this study the channel network shown in Figure 2.3 is functionalized as depicted.
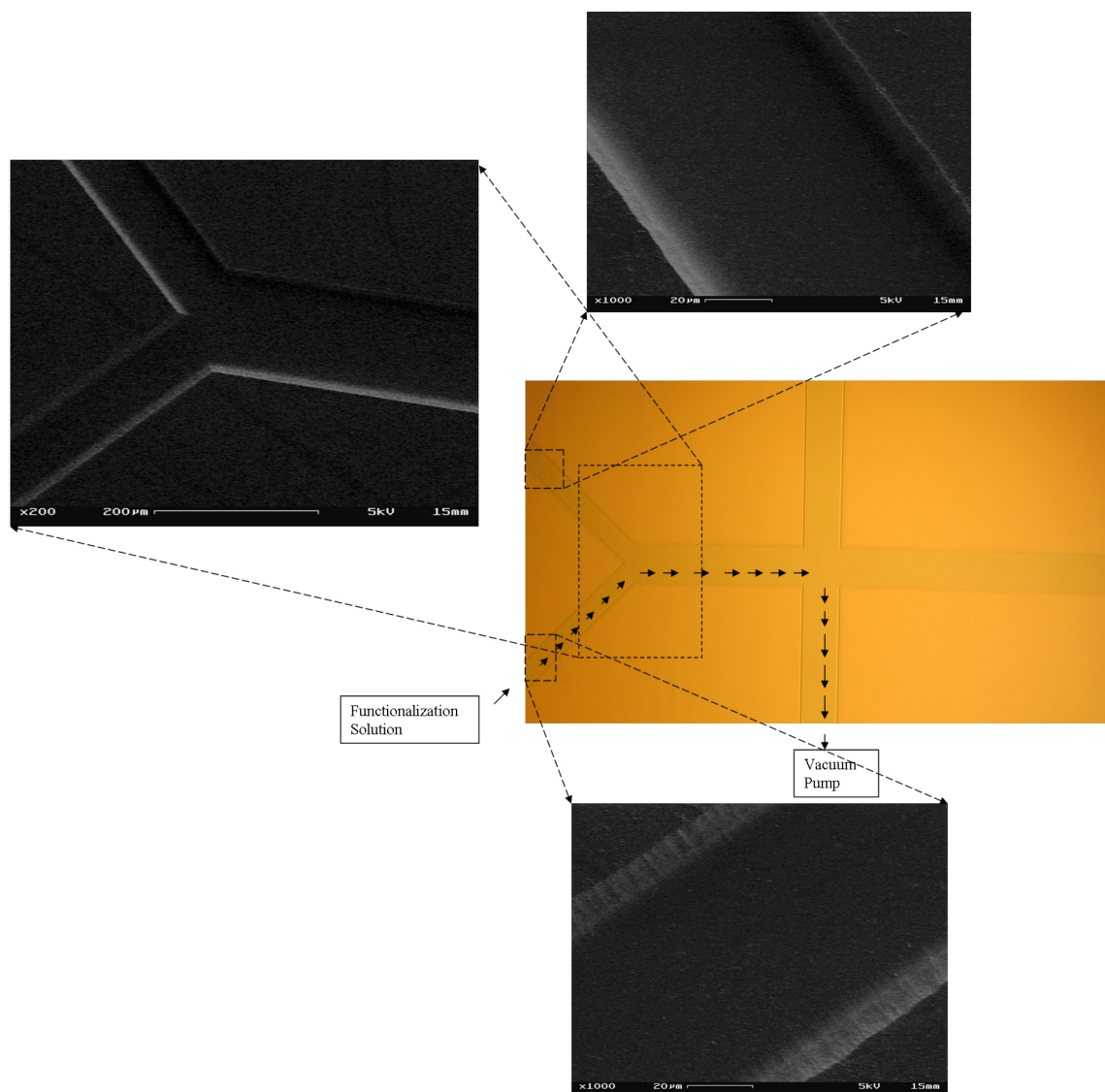
Figure 2.3: Model "Y" shape microfluidic device Scanning Electron Microscopy (SEM) pictures with the illustration of microchannel functionalization

After functionalization, surface characterization is done by contact angle (CA) measurements (Rame-Hart Model 250-00) measured as the advancing angle of a sessile drop of Millipore (18 MΩ) water and X-ray photoelectron spectroscopy (XPS) (PHI Model 5600) to determine the chemical composition of the adherent surface layers.

2.5. Characterization Methods

For the characterization of flat surfaces three techniques were used, X-ray photoelectron spectroscopy (XPS) which provides information about the chemical

composition of the surface, contact angle (CA) measurements which provide information about the surface energy, and atomic force microscopy (AFM) which provides information about the topography of the surfaces.

2.5.1. X-Ray Photoelectron Spectroscopy

X-ray photoelectron spectroscopy (XPS) or electron spectroscopy for chemical analysis (ESCA) is based on the photoelectric effect. In this surface analysis tool, the elemental composition of the molecules on the surface, chemical or electron state of surface elements can be determined. The typical depth of penetration for surface sensitivity is 1– 10 nm.

An X-ray beam is directed to the sample surface in an ultra high vacuum (<10^{-6} Torr) chamber. The irradiation of the surface causes emission of the photoelectrons if the x-ray photon energy is greater than the binding energy of the electron from the atoms of the surface molecules. The kinetic energy (E_k) and intensity of escaped photoelectrons are measured by the energy analyzer. Since the x-ray photon energy (h_v) is known for specific x-ray sources the binding energy (E_b) is determined by:

$$E_b = h_v - E_k \tag{7}$$

For insulating samples due to the emitted photoelectrons, the surface builds up a positive charge on the surface as the excess positive charges do not get conducted away. This excess surface charge reduces the kinetic energy of the emitted electrons, yielding an artificial shift in the binding energy peaks that can lead to erroneous determination of the surface composition. Therefore, calibration of the samples maybe needed. One commonly used base calibration for binding energies is the C (1s) peak at 285 eV. If the surface charge is denoted by C then the relation for the E_b is given by:

$$E_b = h_v - (E_k - C) \tag{8}$$

In the present work, flat sample surfaces were evaluated by the XPS (PHI Model 5600) with an Mg K-alpha (h_v = 1253.6 eV) source. The calculated binding energies were calibrated based on the C (1s) to account for any shift in the binding energies of the observed peaks. Furthermore, KLL Auger peaks are also common in XPS as upon irradiation of with x-rays, some Auger electrons are also emitted. The Auger process can be understood as follows: when an atom is hit by energetic photons, one of the core electrons is emitted, leaving a hole behind. This is an unstable state for the atom. Therefore, an outer shell electron drops down to the hole in the core shells with of the difference in orbital energies being released. If this energy is greater than the binding energy of the outer shell electron, this electron is also emitted and is called the Auger electron. The kinetic energy of the Auger electron (E_{kin}) can be calculated as follows:

$$E_{kin} = E_{CoreState} - E_B - E_C \tag{9}$$

E_B is the energy of the first outer shell and E_C is the energy of the second outer shell. The energy levels are denoted with K for the core level hole, L is for the first outer shell electrons in the initial or ground state and L is for the emitted second outer electrons initial or ground state.

XPS data for the clean glass slide is presented in Figure 2.3. Figure 2.3 shows the baseline information for the flat unmodified glass (SiO_2) surface that will be chemically modified for subsequent experiments. After modifications, the changes in the peaks and new peaks from the adherent surface layers can be identified to confirm successful surface modification.
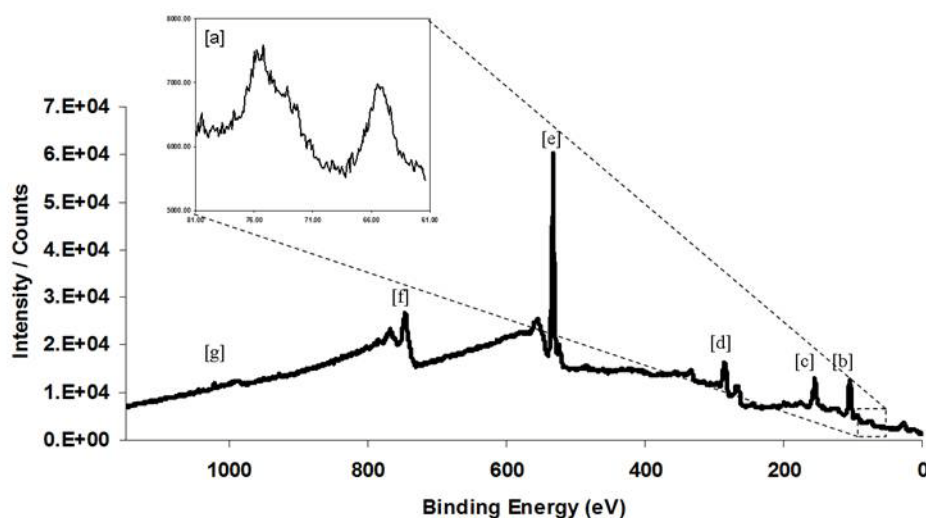
Figure 2.4: XPS spectrum of cleaned bare glass surface. The peaks in the spectrum are; [a] Al (75 eV), Na (64 eV), [b] Si 2p, [c] Si 2s, [d] C 1s, [e] O 1s, [f] C KLL, [g] O KLL

In the spectra shown in Figure 2.3 for the unmodified glass O (1040 eV) and C (744 eV) Auger peaks, O (1s) (532 eV), a small C (1s) (285 eV) peak relative to the chemically modified surfaces, Si (2s) (155 eV), Si (2p) (104 eV) peaks were observed. Al peaks were also observed at 75 eV and 65 eV, which correspond to Al (2p3/2) and Na (2s) additives in the glass slides, as also confirmed by the manufacturer.
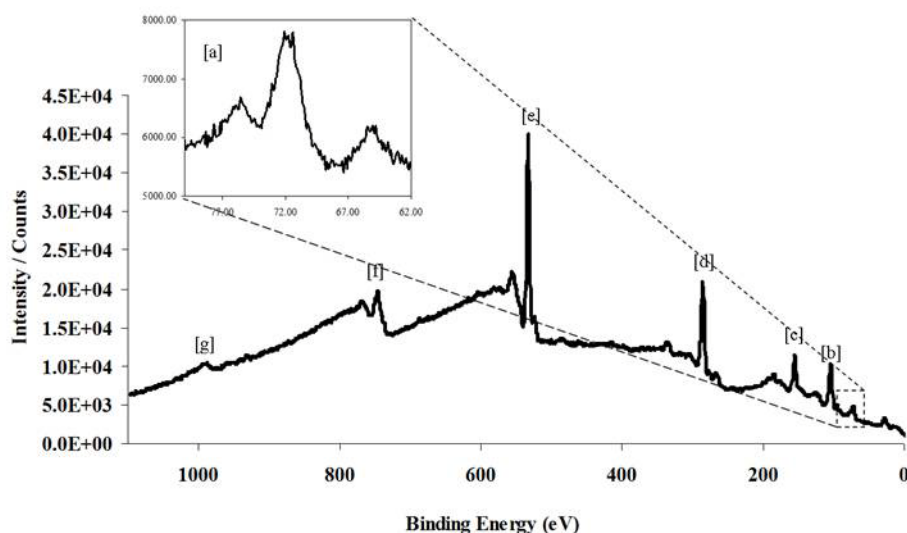
Figure 2.5: XPS spectrum of the –Br terminated surface. The peaks observed are [a] Br 3d which is the characteristic peak for Br termination[b] Si 2p, [c] Si 2s, [d] C 1s, [e] O 1s, [f] C KLL, [g] O KLL

In the next spectrum shown in Figure 2.4, the chemically modified glass slides (Fisher Scientific, 12-540C) with 11-bromoundecyltrichlorosilane (BUTS; Gelest, Inc., Morrisville, PA) is presented. Comparing data in Figs. 2.3 and 2.4, an increase in the intensity of the C (1s) peak was observed. This can be correlated to the hydrocarbon backbone of the attached surface layer which is presented in Fig. 2.5.
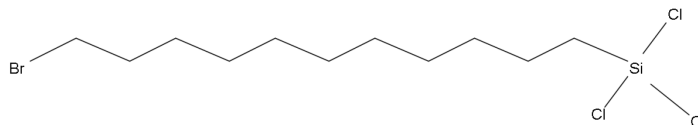
Figure 2.6: Molecular schematic for the structure of BUTS

Furthermore, a Br (3d) peak was observed at 71 eV as shown in the inset to Fig. 2.4.
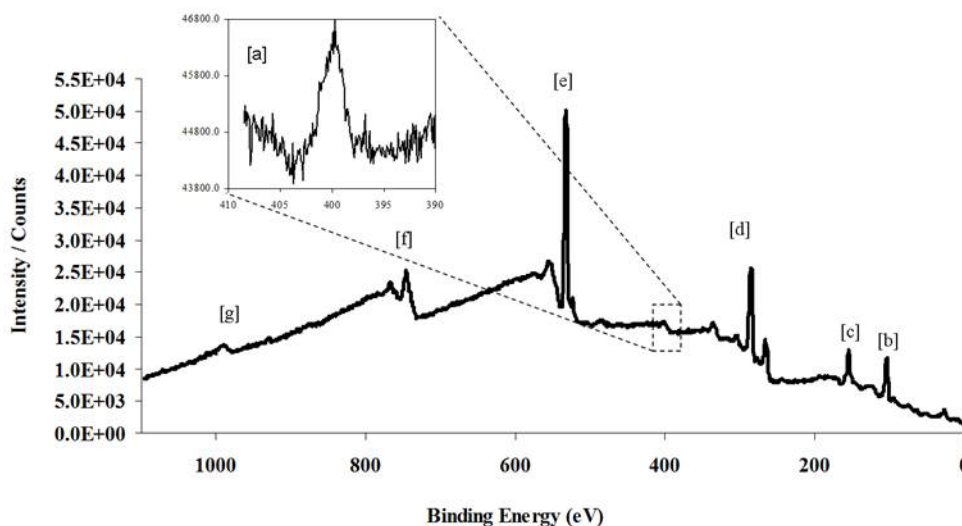
Figure 2.7: XPS spectrum of the azide terminated flat surfaces. The peaks observed are [a] N 1s which is the characteristic peak for azide termination, [b] Si 2p, [c] Si 2s, [d] C 1s, [e] O 1s, [f] C KLL, [g] O KLL

In the next spectrum shown in Fig. 2.6 the azide terminated glass surface is presented. Comparing data in Figs 2.4 and 2.6, a new peak at 400 eV N (1s) and loss of Br (3d) peak was observed. This can be correlated to the S_N2 nucleophilic substitution replacement with the surface bromo groups.
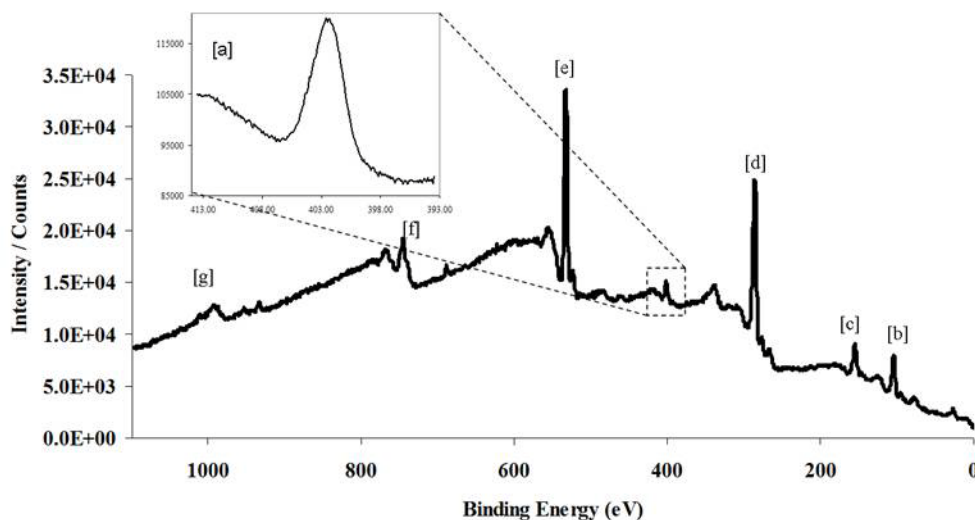
Figure 2.8: XPS spectrum of the −NH$_2$ terminated flat surfaces. The peaks observed are [a] N 1s which is the characteristic peak for amine termination, [b] Si 2p, [c] Si 2s, [d] C 1s, [e] O 1s, [f] C KLL, [g] O KLL

In the next spectrum shown in Fig. 2.7 the −NH$_2$ terminated glass surface is presented. Comparing data in Figs 2.6 and 2.7, an increase in the intensity of the C (1s) and the N (1s) peak at 400 eV was observed. This can be correlated to the "Click" chemistry modification of the surface with −NH$_2$ groups.
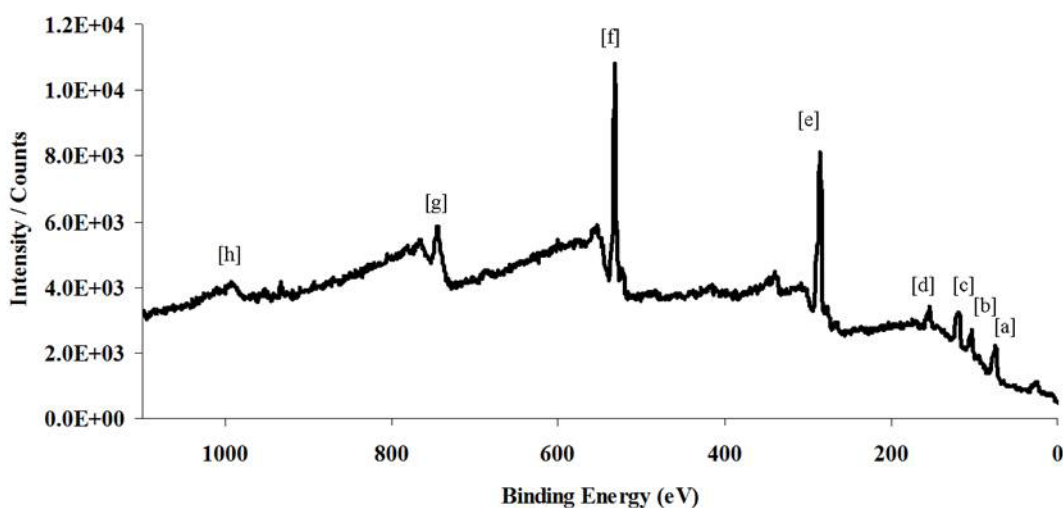
Figure 2.9: XPS spectrum of the −CH$_3$ terminated flat surfaces. The peaks observed are [a] Al 2p3/2, [b] Si 2p, [c] Al 2s, [d] Si 2s, [e] C 1s, [f] O 1s, [g] C KLL, [h] O KLL

In the next spectrum shown in Fig. 2.8 the –CH$_3$ terminated glass surface is presented. Comparing data in Figs 2.6 and 2.8, a loss in the N (1s) peak and an increase in the C (1a) peak was observed. This can be correlated to the "Click" chemistry modification of the surface with –CH$_3$ groups.

2.5.2. Contact Angle Measurements

The contact angle measurements were carried out by using a Ramé-Hart Model 250-00 goniometer as the advancing contact angle of a sessile drop of Millipore (18 MΩ) water. The contact angle for each surface termination is presented on Table 1.

Table 2.1: Advancing contact angle of adhered surface layers

Θ_{adv} (deg) (–Br)	Θ_{adv} (deg) (–N$_3$)	Θ_{adv} (deg) (–NH$_2$)	Θ_{adv} (deg) (–CH$_3$)
87.9 ± 2.9	74.2 ± 2.1	69.5 ± 3.6	108.3 ± 3.1

Contact angle is a measure of surface energy. Young's equation gives the relation between the surface energy of a surface and the contact angle

$$\gamma_{SL} + \gamma_{LV} Cos\theta_C = \gamma_{SV} \tag{10}$$

γ_{SL}, γ_{LV} and γ_{SV} are respectively the solid/liquid interfacial tension, liquid/gas interface tension and solid/gas interface tension. Young's relation for the contact angle and surface energy assumes that the surface is a smooth line. For hydrophobic surfaces, Cassie and Wenzel models account for the surface roughness as described next.
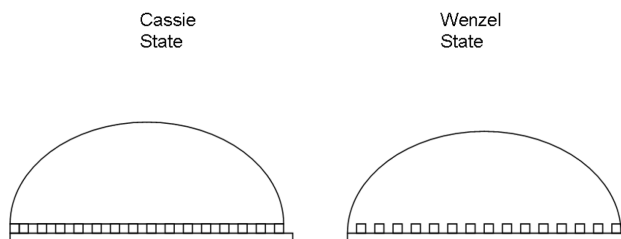
Figure 2.10: Cassie and Wenzel State for sessile drop on hydrophobic surfaces

Cassie's model describes the effective contact angle for the composite surfaces. As shown in Figure 2.9, the composite surface consists of air and solid surface. The Cassie relation for a composite surface is given by:

$$Cos\,\theta_C = \gamma_1 Cos\,\theta_1 + \gamma_2 Cos\,\theta_2 \tag{11}$$

where θ_C is the effective contact angle, γ_1, θ_1 are the areal fraction and contact angle for component 1 and γ_2, θ_2 are the areal fraction and contact angle for component 2. In the Cassie model, since component 2 is air, $Cos(180°) = -1$ and therefore from equation (7),

$$Cos\,\theta_C = \gamma_1 (Cos\,\theta_1 + 1) - 1 \tag{12}$$

If bare glass surfaces are assumed to be smooth then θ_1 would be 2°. For clean glass surfaces the measured contact angle was 2°. The areal fractions of air trapped under the drop for –Br and –NH$_2$ terminated surface were calculated from equation (7) and are summarized in Table 2.

Table 2.2: Aerial fractions of solid under the sessile drop for –Br, –NH$_2$, and –CH$_3$ terminated surfaces

γ_{Br}	γ_{NH_2}	γ_{CH_3}
0.52	0.68	0.35

The trend observed in the data set that shows the trapped air under the sessile drop is increasing when the surface changes from hydrophilic to hydrophobic. This means that for the –NH$_2$ adhered layer surface groups are closely packed trapping least amount of air respect to other surfaces. But, for –CH$_3$ terminated surface the surface groups are sparsely formed with trapping most amount of air with respect to other surfaces.

Wenzel's model the measures contact angles as function of roughness factor in contrast to the contact angle for a smooth surface. The Wenzel relation is given as

$$Cos\theta^* = rCos\theta \qquad\qquad (13)$$

where θ^* is the measured contact angle, r is the roughness factor, and θ is the contact angle for a smooth surface. The surface roughness factors for –Br, –NH$_2$, and –CH$_3$ terminated surfaces are presented in Table 2.3.

Table 2.3: Roughness factors for –Br, –NH$_2$, and –CH$_3$ terminated surfaces

r_{Br}	r_{NH_2}	r_{CH_3}
0.0367	0.3504	-0.3092

The roughness factor represents the roughness level with respect to clean bare glass at 2° of advancing contact angle. The roughness factor changes from 1 to -1 stating clean bare glass surface (CA=2°) to highly hydrophobic surfaces (CA> >90°). The –CH$_3$ has a negative roughness number stating that the surface is hydrophobic nature. –Br surface has a roughness number that is close to zero. When the number is zero than the surface is not hydrophilic anymore but the surface is not also hydrophobic.

2.5.3 Atomic Force Microscopy

Atomic force microscopy (AFM, Quesant Q-Scope-350) was used to image the functionalized surfaces after functionalization. AFM is a scanning probe technique method that allows surface scanning with microscale cantilever with various radii of curvature tips for various applications. There are two modes for surface scanning, contact and tapping mode which is a non-contact mode. AFM scans provide the ability to directly create images of the surface topography and can be used to identify the surface coverage and a qualitative measure of the modified surfaces.

In the contact mode the tip of the AFM cantilever is in contact with the surface. During the scan, due to the surface topography the cantilever deflects and creates a

feedback signal which translates to a surface image. In the tapping mode, the cantilever vibrates at a frequency which is set for each application as setting the spring constant of the cantilever. When the tip approaches the surface at an atomic height level and starts moving over the surface in one direction. Due to the Van-der Waals forces between the tip and the surface changes the frequency of the cantilever which gives out a feedback signal. The feedback signal translates to image of the surface. The non-contact, tapping mode is chosen due to avoid direct friction with modified surfaces and thereby damaging the surface. The AFM images are presented for bare glass surface, $-Br$, $-NH_2$, and $-CH_3$ terminated surfaces below in Figs. 2.10. Comparing data in 2.10 [b] and 2.10 [a], a significant increase in the roughness was observed. But, comparing data in 2.10 [a] and 2.10 [c], the increase in the roughness was also observed. But, comparing 2.10 [c] and 2.10 [b] the decrease in the roughness was observed. Comparing 2.10 [d] to all other surfaces the most significant increase in roughness is observed.

Taking all data into account, confirms that the surface functionalization procedure is successful for terminating glass surfaces with $-Br$, $-NH_2$, and$-CH_3$. Figure 2.2 shows the schematic that depicts the chemical structure of the molecules that form the adherent surface layers.
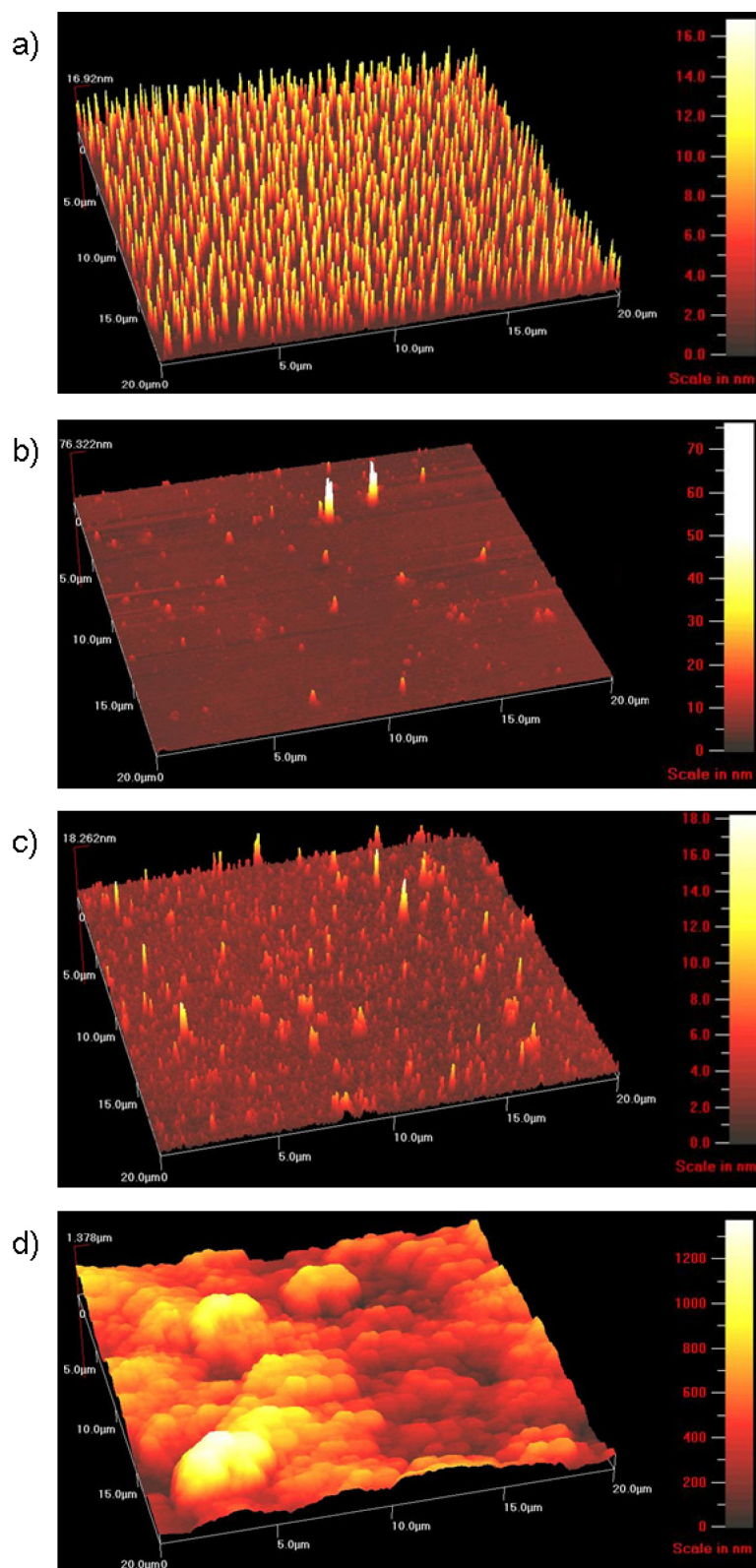
Figure 2.11: AFM surface scan (20 µm x 20 µm) [a] for clean bare glass, [b] –Br terminated glass, [c] –NH$_2$ terminated glass, [d] –CH$_3$ terminated glass

2.6. Experimental Methods

2.6.1 Stability Experiments for Flat Surfaces

$-Br$, $-NH_2$, and $-CH_3$ terminated surfaces were exposed to various acids, such as Cr etchant (Transene Co., Danvers, MA), Au etchant (Transene Co., Danvers, MA), hydrofluoric acid, sulfuric acid, hydrochloric acid, and piranha solution (4:1 sulfuric acid : hydrogen peroxide) at 60 ºC, basses, such as 400 K developer, NaOH (Sodium Hydroxide), and SC-1 cleaning solution at 73 ºC, solvents, such as isopropanol (IPA) and acetone. It should be noted that the piranha solution is strongly oxidizing, and HF is extremely dangerous, so, extreme caution should be taken. Each model substrate was submerged in each chemical for 5 min. followed by DI water soak for 1 min. Then, the samples were rinsed with copious amounts of DI water and dried under a stream of dry N_2.

All three surface adhered layers were exposed to oxidative plasma environment at various powers such as 30 W, 50 W, and 100 W for 5 min., three different thermal exposures by placing in an oven at different temperatures such as at 90 ºC, 150 ºC and 205 ºC, UV light on a mask aligner (Karl Suzz) at different total energies per unit area such as 100 mJ/cm^2, 200 mJ/cm^2, 500 mJ/cm^2, 1000 mJ/cm^2, 1500 mJ/cm^2.

2.6.2. Characterization of Microfluidic Devices

The characterization of model surface-modified microfluidic device was done with fluorescence microscopy (Nikon TE2000). For a voltage source for electroosmotic flow experiments and current-voltage measurements (I-V) an electrometer (Keithley Instruments, Cleveland, Ohio) was used. The microfluidic device was filled with 10 mM phosphate buffer at pH 6.9 +/- 0.1 with ensuring no bubbles formed in channels during

filling. It is important to control the pH of the supporting electrolyte buffer as surface charge is a function of solution pH [64]. Fluorescein, a negatively charged dye at neutral pH (Sigma-Aldrich, St. Louis, MO) and Rhodamine B, a positively charged dye at neutral pH (Sigma-Aldrich, St. Louis, MO) were used as indicator dyes to track the electroosmotic flow during the electrokinetic flow experiments. Electrokinetic experiments were preformed away from Joule heating. The I-V measurements to check the Joule heating range for the device is presented in Appendix 10.

After the microfluidic device was filled with phosphate buffer solution, device was placed on the inverted microscope with electrical connections attached to the reservoirs. The experimental setup is presented in Figure 2.11. A few drops of the indicator dye were injected to the inlet reservoir. Since the fluorescein is a negatively charged dye in neutral pH, a positive field is applied from outlets (+50 V) and *vice versa* for rhodamin b. To excite the fluorescein indicator dye, which has an excitation wavelength of 494 nm, during the electroosmotic flow experiments, a fluorescence light filter with a range of 450 nm – 500 nm is used. And, to excite the rhodamine b indicator dye which has a 540 nm excitation level, fluorescence light filter with a range of 530 nm – 560 nm is used.
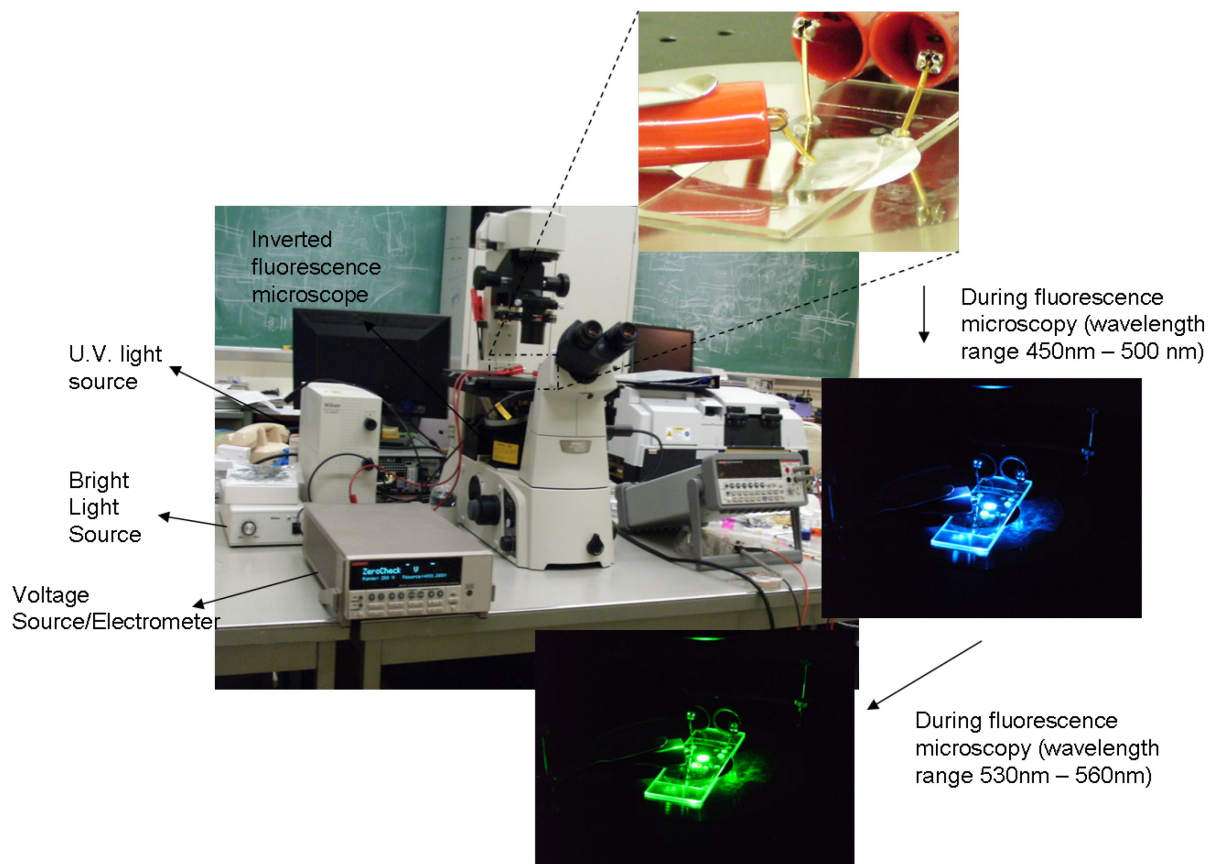
Figure 2.12: Experimental setup for electroosmotic flow visualization

Chapter 3

Results and Discussion

3.1 Stability Results of Chemically Modified Flat Surfaces

In this section, the stability information for the surface adhered layers, –Br and –NH_2, –CH_3 under microfabrication and working conditions are evaluated and discussed. This data provides direct understanding about layers and the interaction of these layers to many different environmental conditions, as discussed. As a consequence, it is possible to systematically engineer experiments or fabrication processes for surface maximum use of the surface-modified microfluidic devices.

In order to evaluate the stability of the adhered –Br, –NH_2, and -CH_3 terminated surface layers, model substrates were exposed to a large range microfabrication and working conditions in a broad parametric study. After exposure, these model surfaces were characterized by methods described previously. The CA measurements provide a measure of the surface energy and were the first set of measurements conducted. If the surface after exposure shows a change in CA more 10° then XPS characterization was carried out to determine the exact surface chemical composition and to evaluate if the exposure altered the surface layers chemically. If the change is CA was less than 10° then AFM measurements were carried out to confirm if there is a structural change in the adhered surface layers. The least count of the goniometer is 1°. The 10° threshold is chosen for two reasons. First, the uncertainty in the CA measurements can be on the order of 10°, as estimated through repeated statistical measurements at multiple positions on one sample and across multiple samples, which implies that for samples within the uncertainty range it is highly unlikely that the surface layers undergo a significant change

in chemical composition that leads to a change in the surface energy and an observed change in the CA. Second, it is well-known that changes in CA can also arise due to change in the surface roughness (theoretically discussed as the Cassie and Wenzel models); the AFM measurements confirm such changes in the likely absence of changes in chemical composition. If there is a difference in roughness and topography when the change in the CA values are less than 10°, than, orientation of the surface molecules could change with exposure or there is a partial loss of the adhered surface layer. The surfaces were compared to pre-exposure conditions to identify the changes. Changes to either the CA or surface chemical composition points to the lack of stability of the adherent surface layers to various conditions.

3.1.1 Acid Exposures

Table 3.1: Contact angle measurements of $-Br$, $-NH_2$ and $-CH_3$ surface layers before and after acid exposures

	Θ_{adv} (deg) ($-Br$)	Θ_{adv} (deg) ($-NH_2$)	Θ_{adv} (deg) ($-CH_3$)
	87.9 ± 2.9	69.5 ± 3.6	108.3 ± 3.1
Exposure Condition	After Exposure	After Exposure	After Exposure
Cr Etchant	88.9 ± 1.3	65.5 ± 3.4	83.0 ± 4.2
Au Etchant	81.6 ± 1.5	63.9 ± 1.7	92.0 ± 2.0
HF	25.7 ± 1.7	29.1 ± 2.8	19.3 ± 0.1
Sulfuric Acid	79.1 ± 3.0	48.2 ± 7.2	68.4 ± 1.6
HCl (32%)	80.7 ± 1.2	44.2 ± 0.6	81.7 ± 1.7
Piranha Solution	22.5 ± 4.9	13.0 ± 0.1	35.7 ± 7.7

A change in the contact angle values is observed in Table 4 for the $-Br$ terminated surfaces after hydrofluoric acid, piranha solution exposure, Au etchant, sulfuric acid and hydrochloric acid. For the $-NH_2$ terminated surfaces the CA changes after hydrofluoric

acid, sulfuric acid, hydrochloric acid, and piranha solution exposure, and for the $-CH_3$ terminated surfaces the CA changes after all acid exposures. These changes were observed to be beyond the measured statistical uncertainty. The changes in CA suggest that the surface layers have been altered in some way. In most cases, small changes (< 10°) in surface energy as reflected by changes in CA typically reflect changes in surface roughness rather than major changes in surface chemical composition.

When the XPS spectra of the $-CH_3$ terminated surfaces were compared before (Figure 2.8) and after exposure (Figure 3.1.) 10% decrease in the relative peak height of the C (1s) was observed for Cr etchant exposures. But, for Au etchant exposure 25% decrease in the relative height of the C (1s) peak to O (1s) peak height is observed.
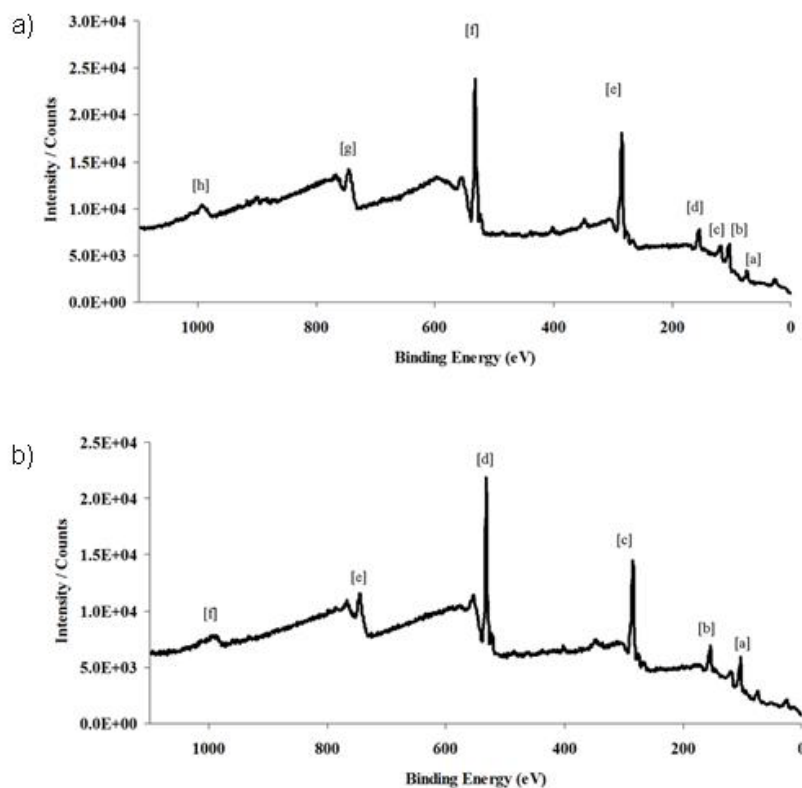
Figure 3.1: XPS spectrum of the **a)** −CH$_3$ terminated flat surfaces after Cr etchant exposure. The peaks observed are [a] Al 2p3/2, [b] Si 2p, [c] Al 2s, [d] Si 2s, [e] C 1s, [f] O 1s, [g] C KLL, [h] O KLL **b)** −CH$_3$ terminated flat surfaces after Au etchant exposure. The peaks observed are [a] Si 2p, [b] Si 2s, [c] C 1s, [d] O 1s, [e] C KLL, [f] O KLL

On the other hand, if the pre-exposure and after exposure AFM scan images are compared (Figures 3.2 and 2.10 [d]) for −CH$_3$ terminated surface then major differences in the topography of the surface are clearly observed. Due to the roughness reduction after Cr etchant exposure in which the roughness factor changed to a low positive value (0.12) means a hydrophilic surface, the CA value is dropped from pre-exposure condition. According to the observations −CH$_3$ terminated surfaces appear to undergo structural changes upon exposure to the Cr etchant. But, after Au etchant surface roughness factor is changed to -0.04 meaning a hydrophobic surface.
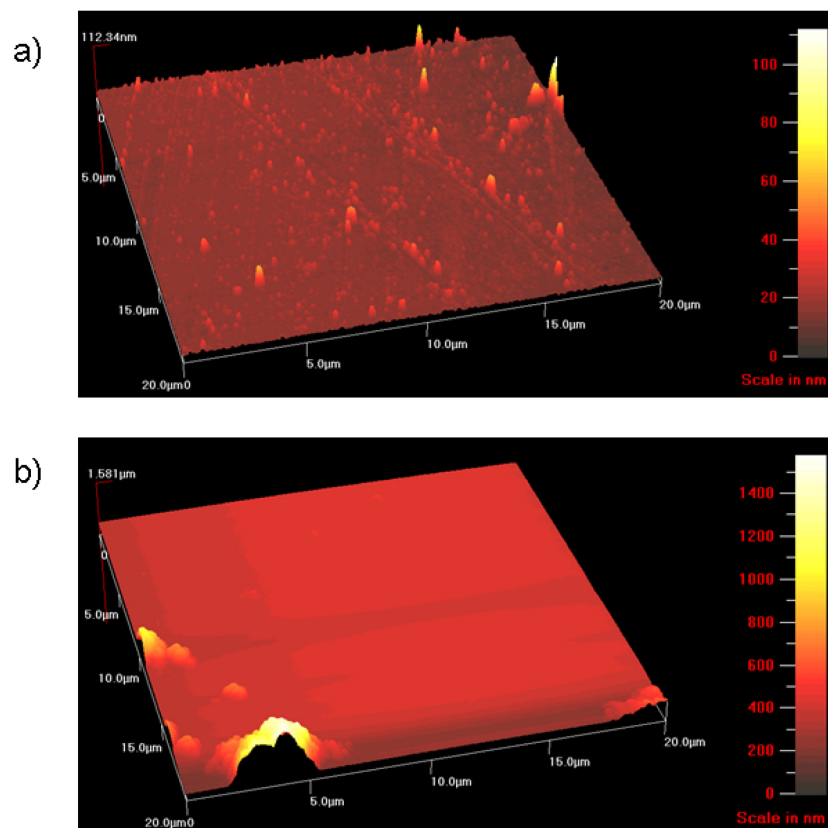
Figure 3.2: AFM surface scan of the –CH₃ terminated surface after **a)** Cr Etchant and **b)** Au Etchant exposure

Hydrofluoric acid or HF is a common chemical used in several microfabrication processes. CA data in Table 4 shows that all three surfaces were influenced by HF.
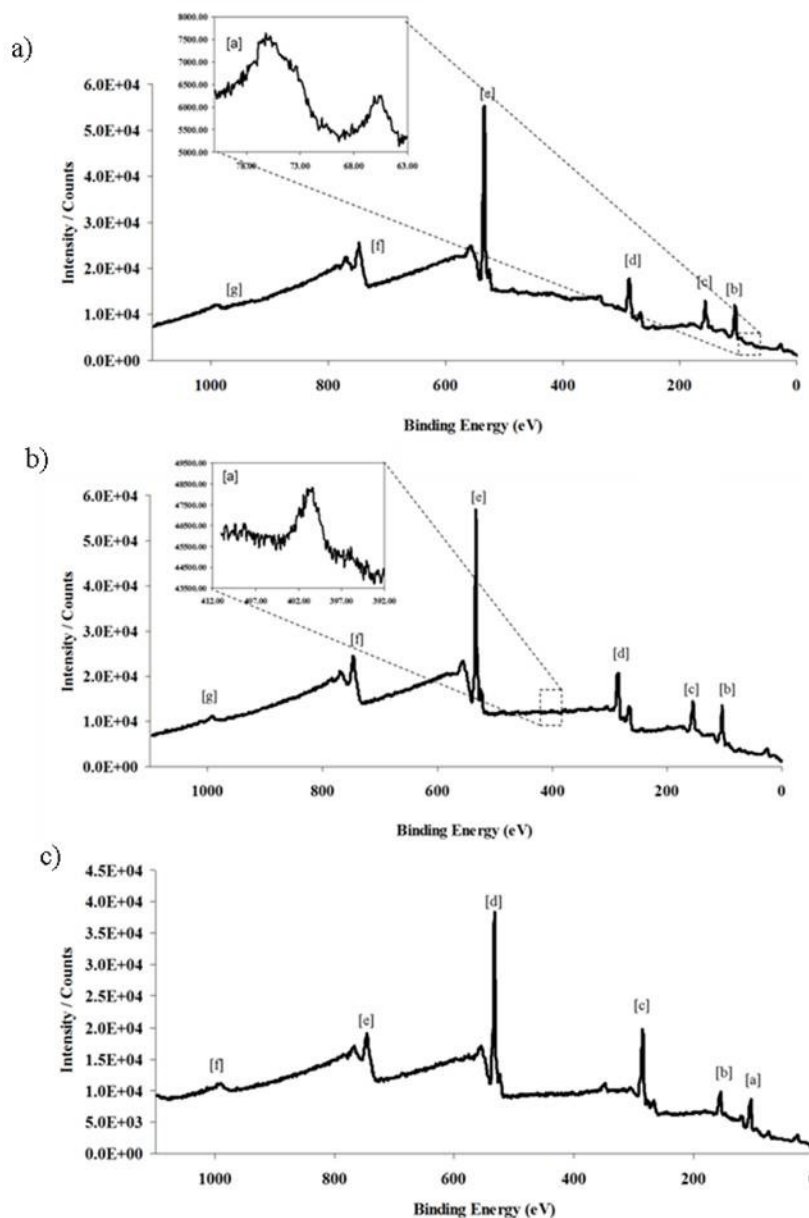
Figure 3.3: XPS spectrum of the **a)** −Br terminated flat surface after HF exposure. The peaks are: [a] Al (75 eV), Na (64 eV), [b] Si 2p, [c] Si 2s, [d] C 1s, [e] O 1s, [f] C KLL, [g] O KLL **b)** XPS spectrum of the −NH$_2$ terminated flat surface after HF exposure. The peaks in the spectrum are; [a] N 1s, [b] Si 2p, [c] Si 2s, [d] C 1s, [e] O 1s, [f] C KLL, [g] O KLL **c)** XPS spectrum of the −CH$_3$ terminated flat surfaces after HF etchant exposure. The peaks observed are [a] Si 2p, [b] Si 2s, [c] C 1s, [d] O 1s, [e] C KLL, [f] O KLL

In the XPS spectra, shown in Figure 3.3 the −Br terminated surface has no Br (3d) signature peak, −NH$_2$ terminated surface N (1s) peak relative intensity decreased %90, and the C (1s) peak relative intensity height is decreased %70. Both the CA and XPS

measurements show significant changes for all three surface layers that HF degrades the

surface layers.
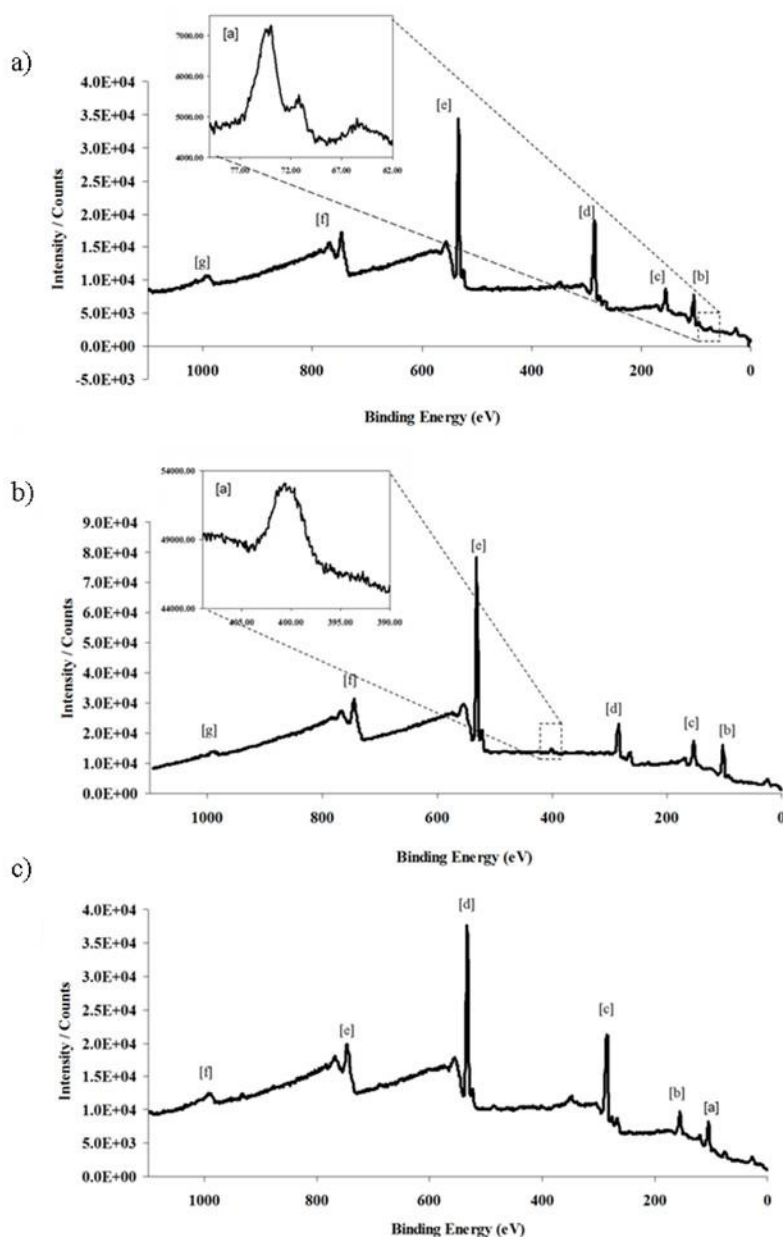
Figure 3.4: XPS spectrum of the after piranha solution exposure for **a)** −Br terminated surface peaks [a] Br 3d, [b] Si 2p, [c] Si 2s, [d] C 1s, [e] O 1s, [f] C KLL, [g] O KLL **b)**– NH$_2$ terminated surface peaks; [a] N 1s, [b] Si 2p, [c] Si 2s, [d] C 1s, [e] O 1s, [f] C KLL, [g] O KLL **c)** −CH$_3$ terminated surfaces peaks [a] Si 2p, [b] Si 2s, [c] C 1s, [d] O 1s, [e] C KLL, [f] O KLL

In the XPS spectra, shown in Figure 3.4 the $-$Br terminated surface has no Br (3d) signature peak, $-$NH$_2$ terminated surface N (1s) peak relative intensity decreased %60, and the C (1s) peak relative intensity height of $-$CH$_3$ terminated surface is decreased %30. Both the CA and XPS measurements show significant changes for all three surface layers that piranha solution degrades the surface layers.

In the XPS spectra, shown in Figure 3.5 $-$NH$_2$ terminated surface N (1s) peak relative intensity decreased %40, and the C (1s) peak relative intensity height of $-$CH$_3$ terminated surface is decreased %10 for sulfuric acid exposure.
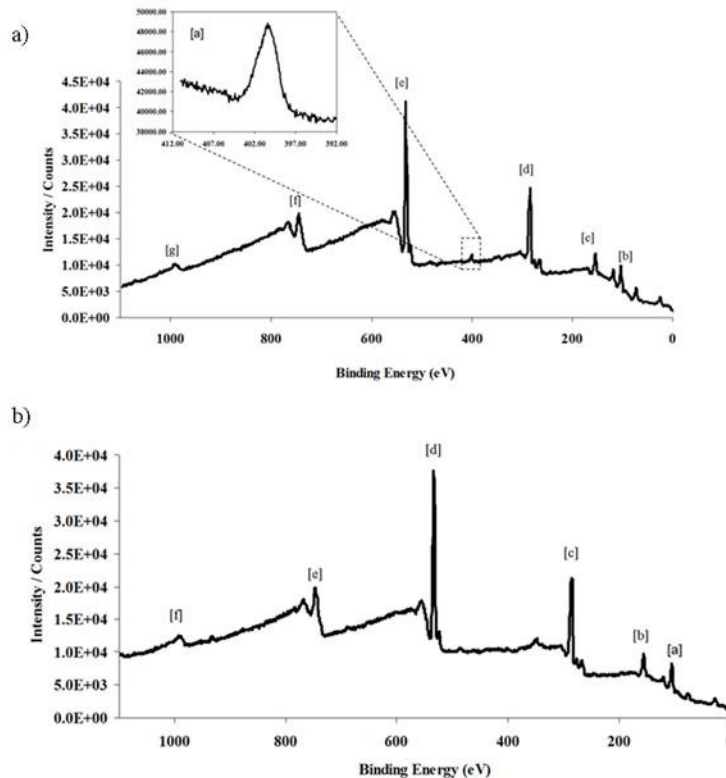
Figure 3.5: XPS spectrum of the **a)** $-$NH$_2$ terminated surface after sulfuric acid exposure. The peaks are: [a] N 1s, [b] Si 2p, [c] Si 2s, [d] C 1s, [e] O 1s, [f] C KLL, [g] O KLL. **b)** XPS spectrum of the $-$CH$_3$ terminated flat surfaces after sulfuric acid exposure. The peaks observed are [a] Si 2p, [b] Si 2s, [c] C 1s, [d] O 1s, [e] C KLL, [f] O KLL

AFM scans were done for $-$Br, $-$NH$_2$, and $-$CH$_3$ terminated surfaces after sulfuric acid exposure. Comparing before and after AFM scans shows that the roughness of the

exposed surface is decreases by approximately 10 nm for –Br, 100 nm for –NH$_2$, 1 μm change for –CH$_3$ terminated surfaces. This could be the reason for the 8°decrease for –Br, 20° decrease for –NH$_2$ and 40° decrease for –CH$_3$ terminated surfaces after exposure CA value.
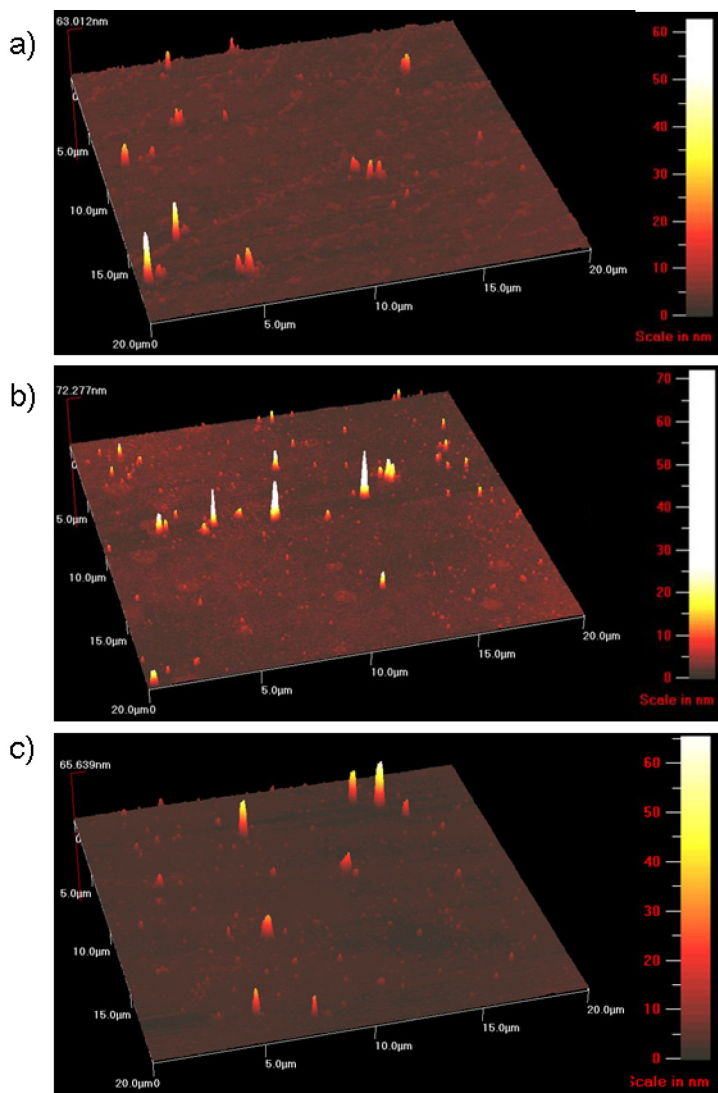
Figure 3.6: AFM surface scan after sulfuric acid exposure after **a)** –Br terminated surface, **b)** –NH$_2$ terminated surface, **c)** –CH$_3$ terminated surface

In the XPS spectra, shown in Figure 3.7 –NH$_2$ terminated surface N (1s) peak relative intensity decreased %22, and the C (1s) peak relative intensity height of –CH$_3$ terminated surface is decreased %10 for sulfuric acid exposure.
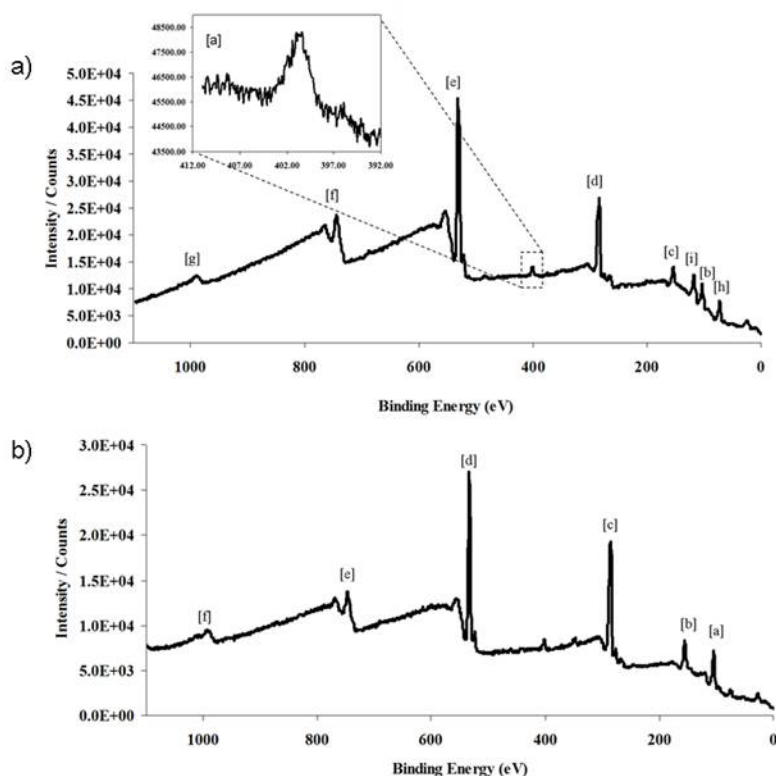
Figure 3.7: XPS spectrum of the **a)** −NH₂ terminated flat surface after HCl exposure. The peaks in the spectrum are; [a] N 1s, [b] Si 2p, [c] Si 2s, [d] C 1s, [e] O 1s, [f] C KLL, [g] O KLL, [h] Al 2p3/2, [i] Al 2s XPS spectrum of the **b)** −CH₃ terminated flat surfaces after HCl exposure. The peaks observed are [a] Si 2p, [b] Si 2s, [c] C 1s, [d] O 1s, [e] C KLL, [f] O KLL

AFM scans were done for −NH₂, and −CH₃ terminated surfaces after hydrochloric acid exposure. Comparing before and after AFM scans shows that the roughness of the exposed surface is decreases by approximately 10 nm for −NH₂, 1 μm change for −CH₃ terminated surfaces. This could be the reason for the 25° decrease for −NH₂ and 27° decrease for −CH₃ terminated surfaces after exposure CA value.
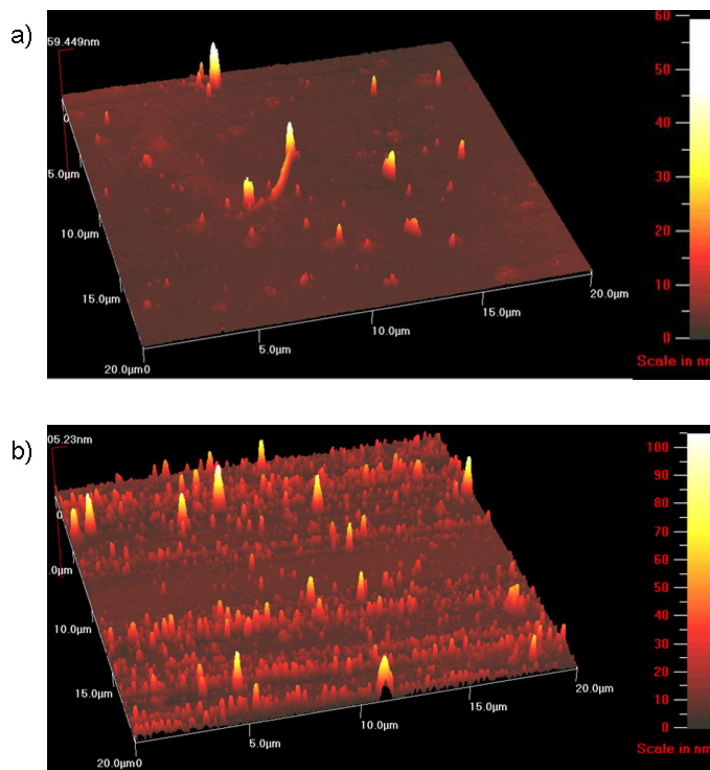
Figure 3.8: AFM surface scan after HCl acid exposure after **a)** –NH$_2$ terminated surface **b)** –CH$_3$ terminated surface

3.1.2. Base Exposure

The CA values for after exposure surfaces for –Br, –NH$_2$, and –CH$_3$ terminated

surfaces are presented at the Table 3.2

Table 3.2: CA values for –Br, –NH$_2$ and CH$_3$ terminated surfaces after exposure to various bases

	Θ_{adv} **(deg) (–Br)**	Θ_{adv} **(deg) (–NH$_2$)**	Θ_{adv}**(deg)(–CH$_3$)**
	87.9 ± 2.9	69.5 ± 3.6	108.3 ± 3.1
Exposure Condition	After Exposure	After Exposure	After Exposure
400K Developer	85.7 ± 1.7	69.6 ± 1.0	111.4 ± 2.4
NaOH	79.1 ± 1.2	51.1 ± 7.4	106.6 ± 1.1
SC-1 Cleaning	89.6 ± 0.6	43.3 ± 2.1	56.0 ± 3.8

There is no significant decrease in the CA values for 400K developer exposure observed in Table 3.2. After the SC-1 exposure of $-NH_2$ and CH_3 terminated surfaces, CA values decreased for 23° and 52°.
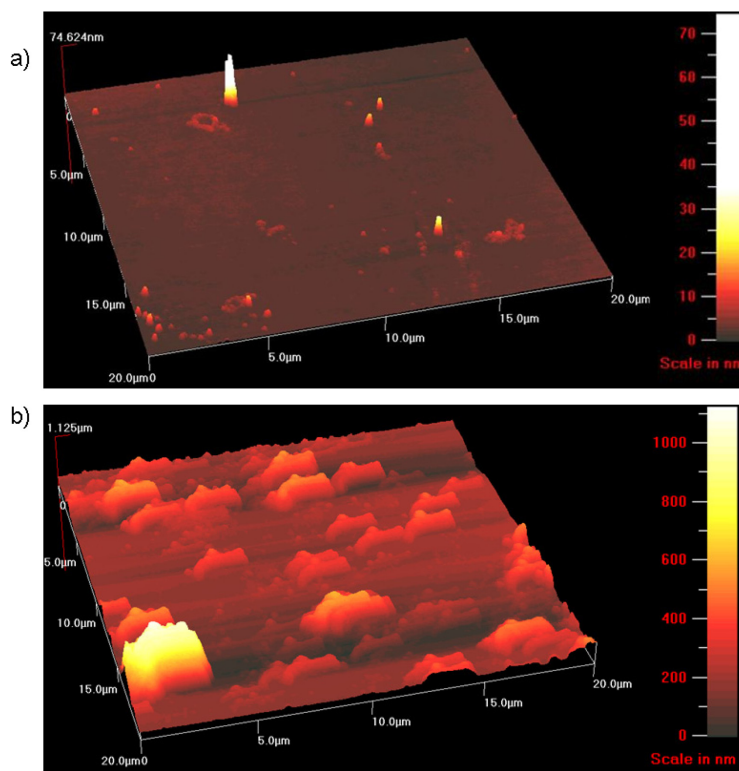
Figure 3.9: AFM surface scan after SC 1 exposure after **a)** $-NH_2$ terminated surface, **b)** $-CH_3$ terminated surface

AFM scans were done for $-NH_2$ and $-CH_3$ terminated surfaces after SC-1 solution exposure. Comparing before and after AFM scans shows that the roughness of the exposed surface is decreases by approximately 60 nm for $-NH_2$, 0.6 µm change for $-CH_3$ terminated surfaces. This could be the reason for the 23° decrease for $-NH_2$ and 52° decrease for $-CH_3$ terminated surfaces after exposure CA value. The residue of the surface adhered layers after exposure is observed.

3.1.3 Exposure of NaCl salt solution at different pHs

The only decrease in CA value beyond the uncertainty is observed for –CH$_3$ surface adhered group after NaCl salt solution at pH 3 and pH 4 exposure. There is no significant change in XPS surface scan.
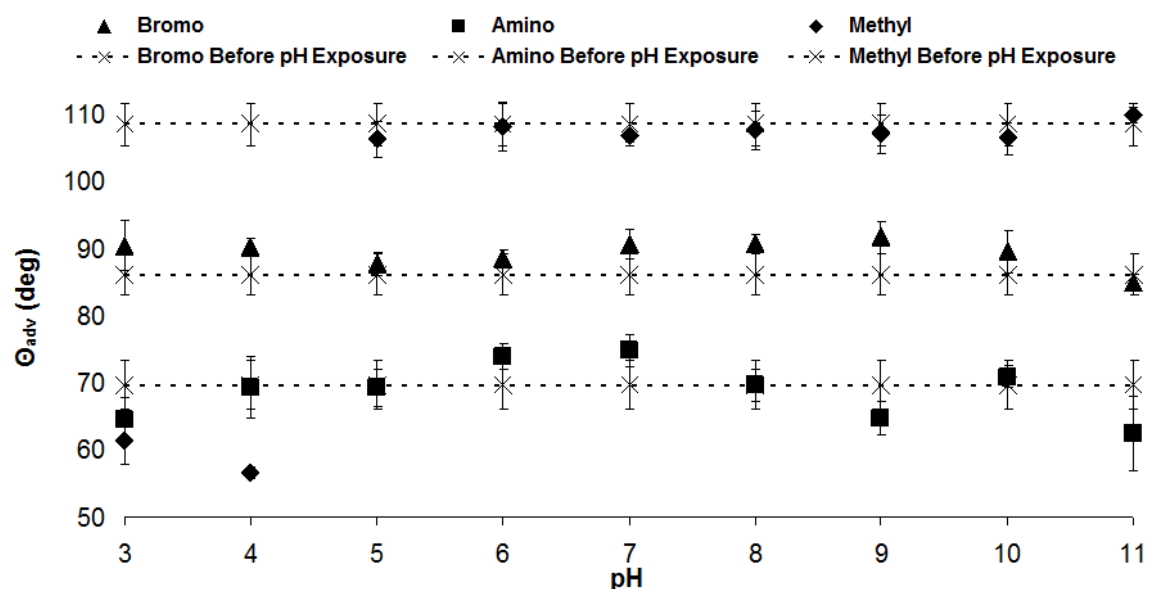
Figure 3.10: CA values for –Br, –NH$_2$ and –CH$_3$ terminated surfaces exposed to NaCl salt solution at various pHs

Comparing before and after AFM scans shows that the roughness of the exposed surface is decreases by approximately 0.5 μm for –CH$_3$ after NaCl solution at pH 3 exposure, and 0.7 μm at pH 4. The instability against the acidic salt solution is a same kind behavior of –CH$_3$ group against an acidic solution.
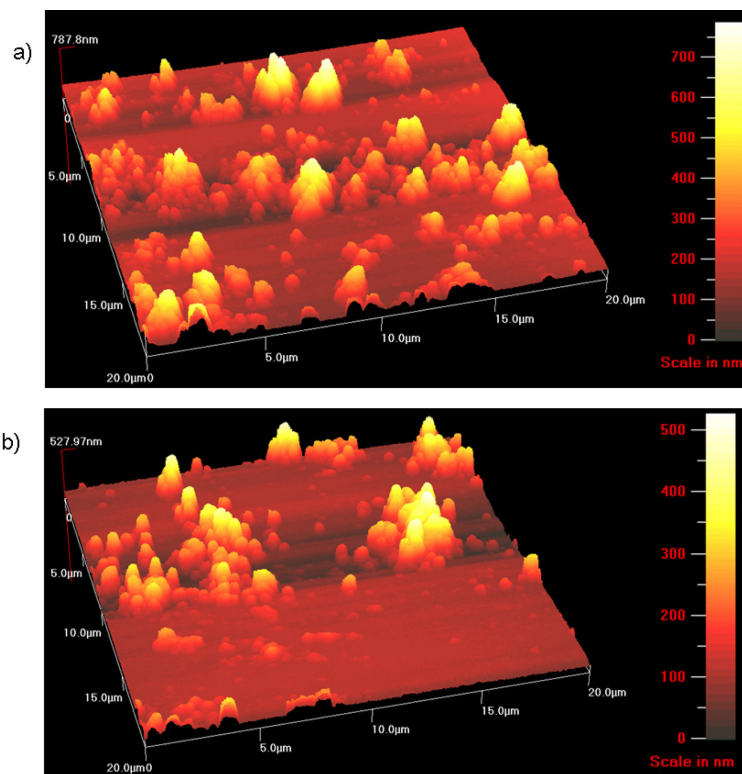
Figure 3.11: AFM surface scan for $-CH_3$ terminated surface after exposure of NaCl salt solution at a) pH 3, b) pH 4

3.1.4. Solvent Exposure

There is no significant change in CA values for $-Br$, $-NH_2$ and CH_3 surface adhered layers after solvent exposures, which is presented in Table 3.3.

Table 3.3: CA values for $-Br$, $-NH_2$ and CH_3 terminated surfaces after exposure to two different solvent

	Θ_{adv} (deg) ($-$Br)	Θ_{adv} (deg) ($-$NH$_2$)	Θ_{adv}(deg)($-$CH$_3$)
	87.9 ± 2.9	69.5 ± 3.6	108.3 ± 3.1
Exposure Condition	After Exposure	After Exposure	After Exposure
Acetone	84.9 ± 1.2	65.3 ± 1.7	109.1 ± 2.1
IPA	88.9 ± 0.9	68.4 ± 1.8	109.1 ± 2.1

3.1.5. Oxidative Plasma Exposure

The after exposure CA values for –Br, –NH$_2$ and –CH$_3$ terminated surface layers is presented in Table 3.4. All surfaces have a significant decrease in CA values after exposure.

Table 3.4: CA values for –Br, –NH$_2$ and –CH$_3$ terminated surfaces after exposure Oxygen Plasma environment

	Θ_{adv} (deg) (–Br)	Θ_{adv} (deg) (–NH$_2$)	Θ_{adv}(deg)(–CH$_3$)
	87.9 ± 2.9	69.5 ± 3.6	108.3 ± 3.1
Exposure Condition	After Exposure	After Exposure	After Exposure
30 Watt	25.8 ± 0.1	24.3 ± 0.9	56.6 ± 5.0
50 Watt	25.9 ± 0.0	22.7 ± 0.0	47.6 ± 5.8
100 Watt	32.8 ± 5.4	26.4 ± 0.1	64.9 ± 5.3

In the XPS spectra, shown in Figure 3.11 the –Br terminated surface has no Br (3d) signature peak, –NH$_2$ terminated surface has no N (1s) peak on survey scan, and the C (1s) peak relative intensity height is decreased %30. Both the CA and XPS measurements show significant changes for all three surface layers that 30 W O$_2$ degrades the surface layers.

Comparison of before and after AFM scans which is presented in Figure 3.12 shows that the roughness of the exposed surface decreases by approximately 1 μm for –CH$_3$ after 30 W, 50 W, and 100 W O$_2$ plasma exposures. Higher CA value than clean bare glass CA value, high C (1s) intensity peak and AFM scans show that after plasma exposures –CH$_3$ terminated surfaces leave residue behind.
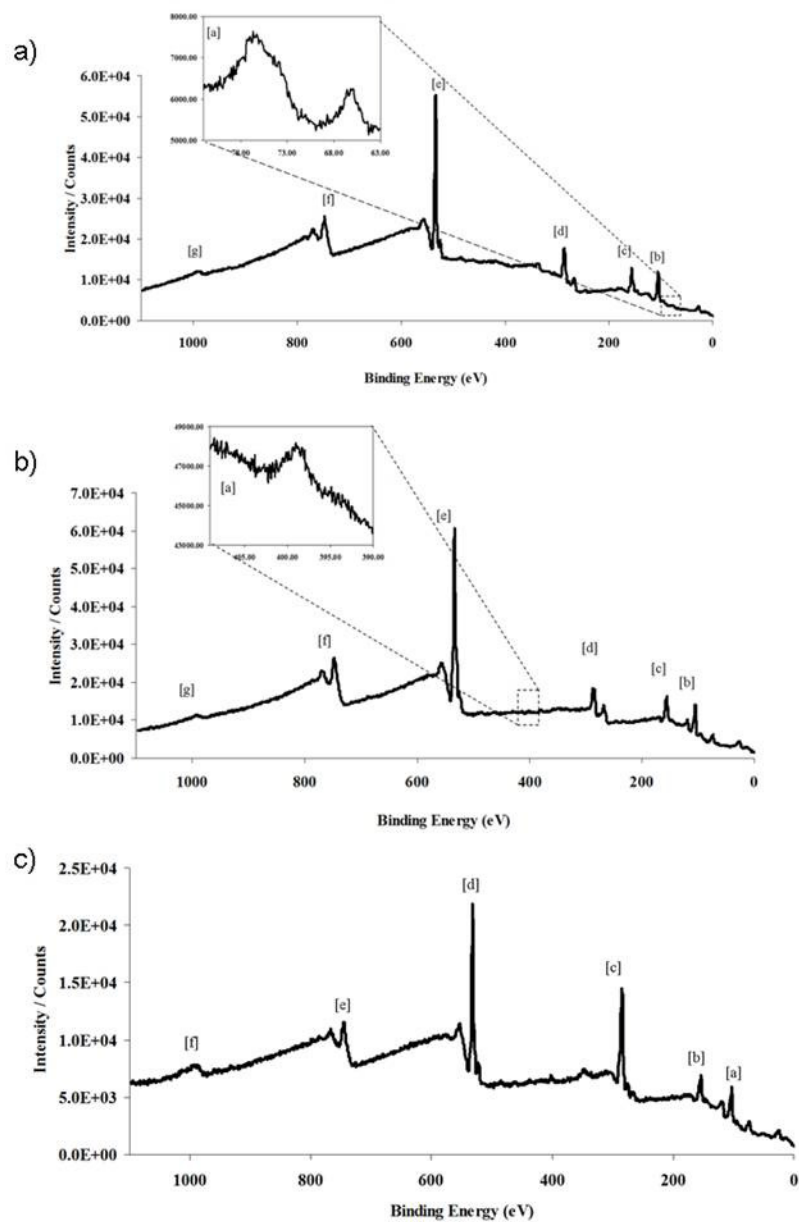
Figure 3.12: XPS spectrum of surfaces after 30 W O_2 plasma exposure for **a)** –Br terminated flat surfaces. The peaks are: [a] Al (75 eV), Na (64 eV), [b] Si 2p, [c] Si 2s, [d] C 1s, [e] O 1s, [f] C KLL, [g] O KLL **b)** –NH_2 terminated flat surface. The peaks in the spectrum are; [a] N 1s, [b] Si 2p, [c] Si 2s, [d] C 1s, [e] O 1s, [f] C KLL, [g] O KLL **c)** –CH_3 terminated flat surfaces. The peaks observed are [a] Si 2p, [b] Si 2s, [c] C 1s, [d] O 1s, [e] C KLL, [f] O KLL
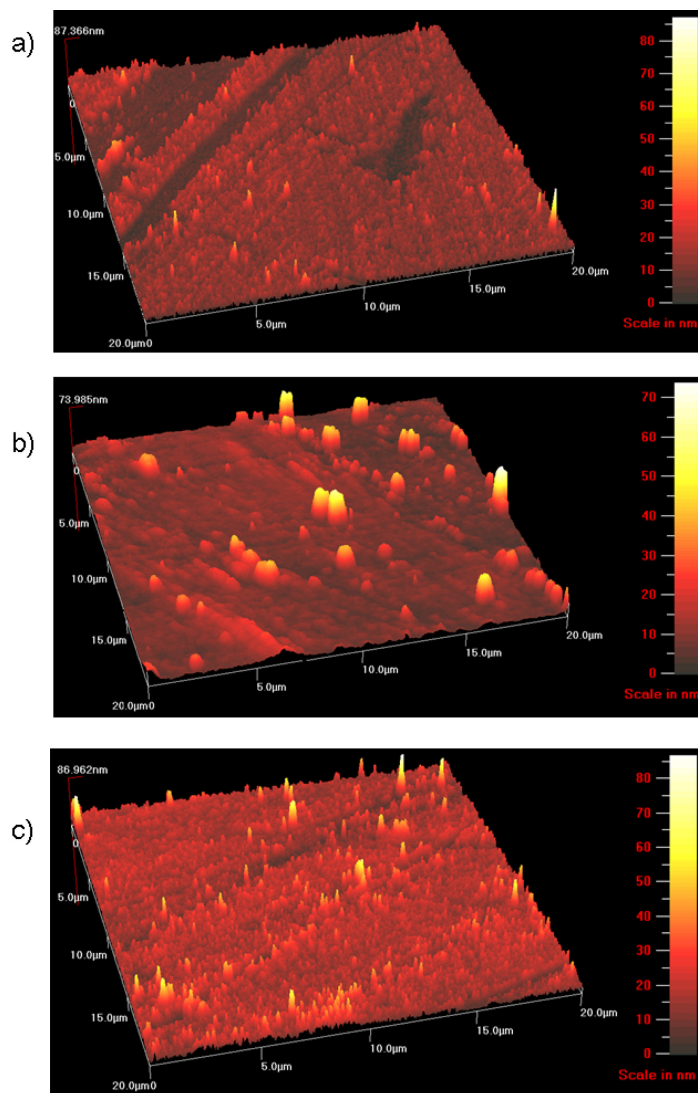
Figure 3.13: AFM surface scan for –CH$_3$ terminated surface after O$_2$ plasma exposure at **a)** 30 W, **b)** 50 W, and **c)** 100 W

3.1.6. Thermal Exposure

The after exposure CA values for –Br, –NH$_2$ and –CH$_3$ terminated surface layers is presented in Table 3.4. All surfaces have a significant decrease in CA values after exposure.

Table 3.5: CA values for –Br, –NH₂ and –CH₃ terminated surfaces after thermal exposures

	Θ_{adv} (deg) (–Br)	Θ_{adv} (deg) (–NH₂)	Θ_{adv}(deg)(–CH₃)
	87.9 ± 2.9	69.5 ± 3.6	108.3 ± 3.1
Exposure Condition	After Exposure	After Exposure	After Exposure
90 ºC	92 ± 2.6	71.7 ± 0.0	104.9 ± 0.1
150 ºC	90.2 ± 1.5	66.3 ± 1.8	102.4 ± 1.4
205 ºC	83.6 ± 0.6	68.6 ± 5.2	74.5 ± 5.3

Only –CH₃ terminated surfaces after 150 ºC and 205 ºC exposures have a significant decrease in the CA value. XPS and AFM scans are presented in Figure 3.13 and 3.14.
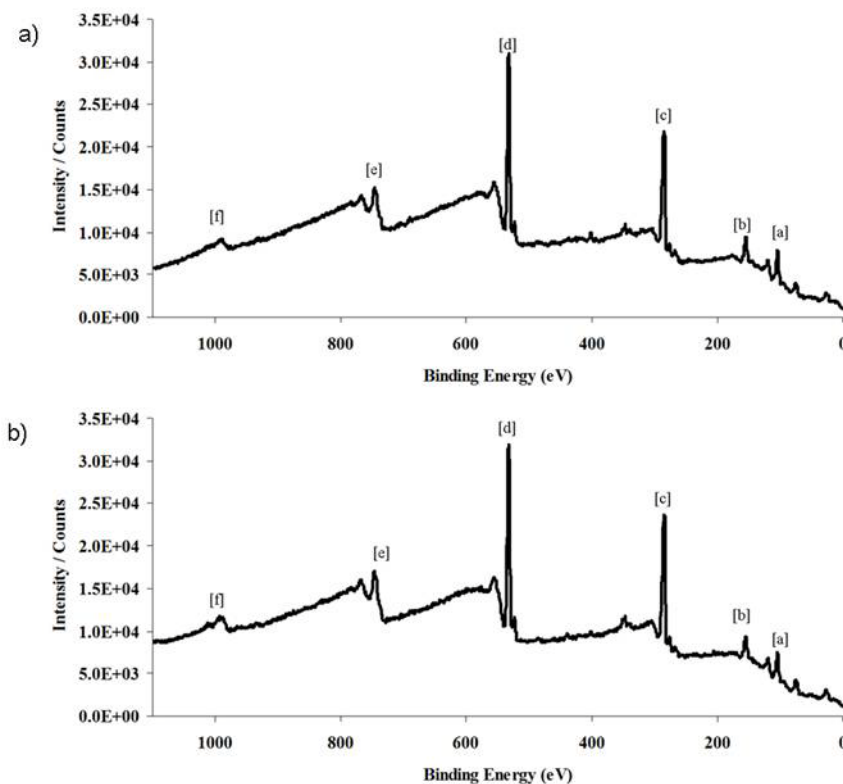
Figure 3.14: XPS spectrum of the –CH₃ terminated flat surfaces **a)** after 150 ºC exposure. The peaks observed are [a] Si 2p, [b] Si 2s, [c] C 1s, [d] O 1s, [e] C KLL, [f] O KLL XPS spectrum of the –CH₃ terminated flat surfaces **b)** after 150 ºC exposure. The peaks observed are [a] Si 2p, [b] Si 2s, [c] C 1s, [d] O 1s, [e] C KLL, [f] O KLL

There is no significant change in XPS scans presented in Figure 3.13. The chemical composition of the surface does not change with thermal exposure.

Comparing before and after AFM scans which is presented in Figure 3.14 shows that the roughness of the exposed surface decreases by approximately 0.3 μm after 150 ºC and 0.5 μm after 205 ºC exposure for $-CH_3$ terminated surface. AFM scans show that after exposure surface adhered layer is not densely packed anymore.
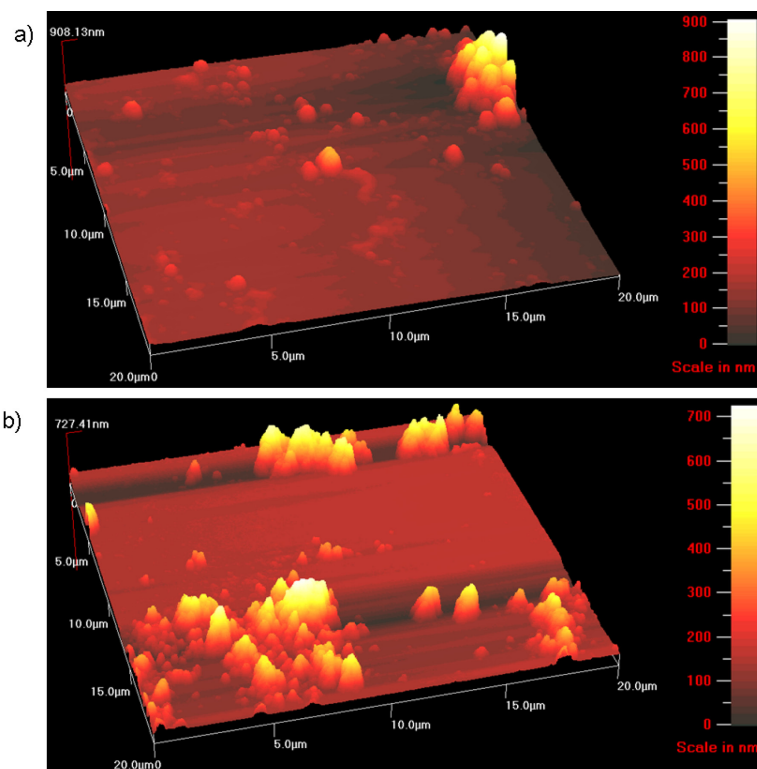
Figure 3.15: AFM surface scan for $-CH_3$ terminated surface after **a)** 150 ºC, **b)** 205 ºC

3.1.7. UV Light Exposure

The CA values for $-Br$, $-NH_2$ and $-CH_3$ terminated surfaces after UV light exposures shown in Table 3.6.

Table 3.6: CA values for –Br, –NH$_2$ and –CH$_3$ terminated surfaces after UV light exposures

	Θ_{adv} (deg) (–Br)	Θ_{adv} (deg) (–NH$_2$)	Θ_{adv}(deg)(–CH$_3$)
	87.9 ± 2.9	69.5 ± 3.6	108.3 ± 3.1
Exposure Condition	After Exposure	After Exposure	After Exposure
100 mJ/cm^2	89.8 ± 0.9	69.7 ± 1.9	108.3 ± 6.6
200 mJ/cm^2	84.4 ± 1.2	67.0 ± 0.9	106.0 ± 1.0
500 mJ/cm^2	86.7 ± 2.1	70.5 ± 2.0	105.8 ± 1.1
1000 mJ/cm^2	87.8 ± 0.4	70.2 ± 0.5	106.0 ± 1.3
1500 mJ/cm^2	84.4 ± 0.3	65.3 ± 1.1	110.2 ± 1.2

Comparing CA values for –Br, –NH$_2$ and –CH$_3$ terminated surfaces after UV light exposures to pre-exposure values no significant change is observed.

3.2 Electroosmotic Flow Directing

The electroosmotic flow directing images with intensity graphics are presented in Figure 3.15 and 3.16. The images are quantified to graph the intensities along the channels with ImageJ software. The Figures 3.15 and 3.16 shows the electrokinetic flow directing for Rhodamine B and Fluorescein dye electroosmotic flow with four different time steps, which shows the evolution of the electrokinetic flow directing with the surface modification method. Also, in Figures 3.15 and 3.16 at each time step the graph of the intensity value of dyes along the center line for both channels is presented.

As shown in intensity graphs, in time, the center line intensity of the Rhodamine B along the surface modified channel disappears before the dye intensity disappears in the native glass surface channel which is due to zeta potential difference between channels. The same phenomenon observed for the Fluorescein dye but in opposite channels due to the opposite charges that dyes have.
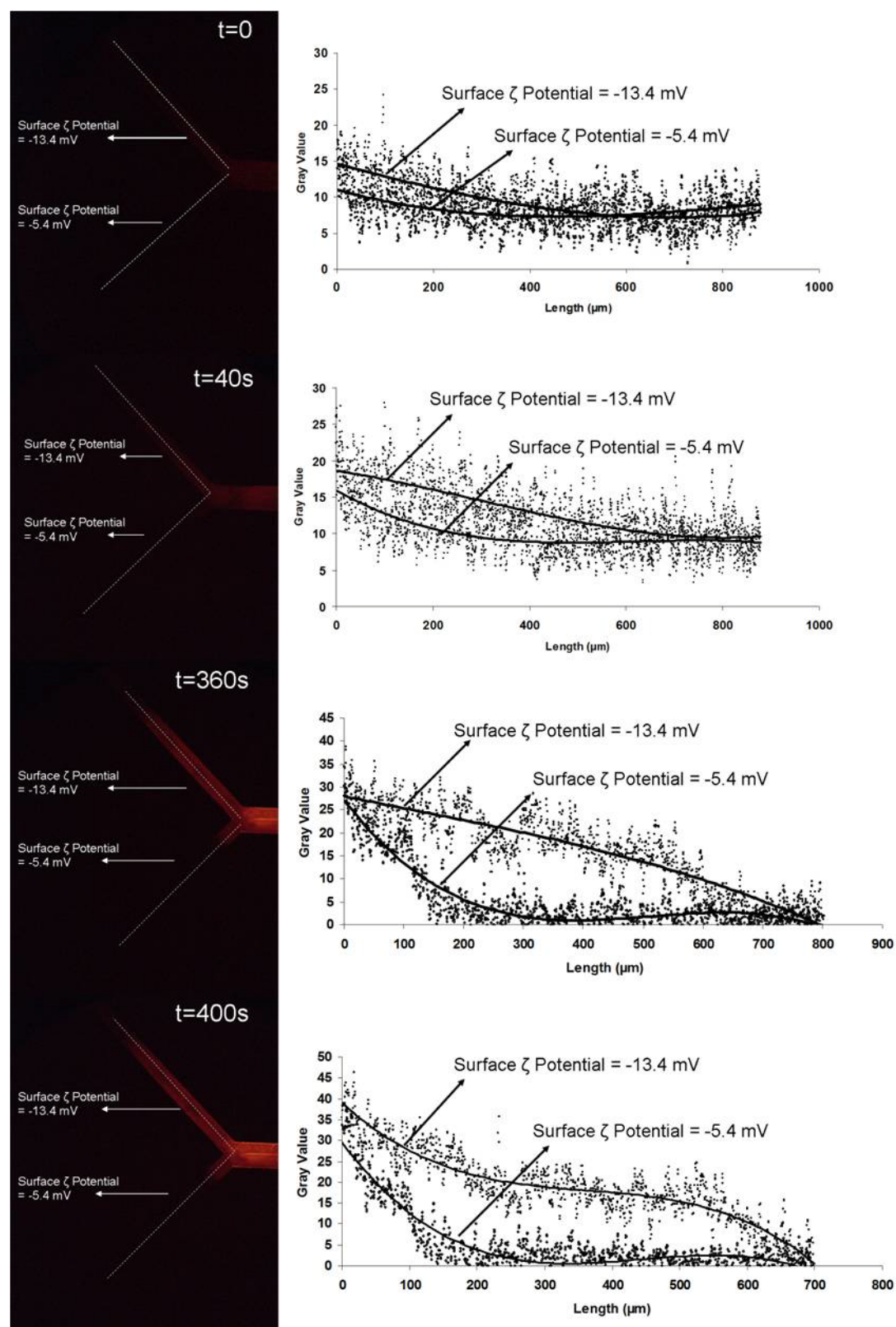
Figure 3.16: Flow directing images of the Rhodamine B dye with intensity graphs along the center line in the channel

Surface charge density is measured by Wu *et. al.*[64] for –Br, –NH$_2$ and –CH$_3$ terminated surface layers. The calculated surface zeta potential for the clean bare glass surface and –NH$_2$ terminated surface are -5.4 mV and -13.4 mV. The ratio of the surface zeta potential for –NH$_2$ terminated surface and the native glass surface is 0.4.

As presented in Table 3.7 the Rhodamine B average intensity value ratios for the average intensity value in the surface modified channel with -5.4 mV surface zeta potential channel, and in the native glass channel with -13.4 mV surface zeta potential channel starts with 0.88 at t=0 and reach to 0.52 at t=400s. This suggests that at t=400s there is 1.92 times higher Rhodamine B dye intensity in native glass channel compared to the Rhodamine B dye intensity in –NH$_2$ terminated channel which is due to the higher electroosmotic flow rate of Rhodamine B in the native glass channel. The higher electroosmotic flow rate of the Rhodamine B dye in native glass channel is due to the higher surface zeta potential for the dye which relates to electroosmotic flow rate of the dye with equations (2) and (3).

Table 3.7: Average intensity values of the Rhodamine B dye in channels

	Channel (-13.4 mV) Average Intensity (Gray Value)	Channel (-5.4 mV) Average Intensity (Gray Value)
Rhodamine B (t=0)	9.35	8.23
Rhodamine B (t=40 s)	13.03	10
Rhodamine B (t=360 s)	21.61	11.57
Rhodamine B (t=400 s)	24.09	12.61
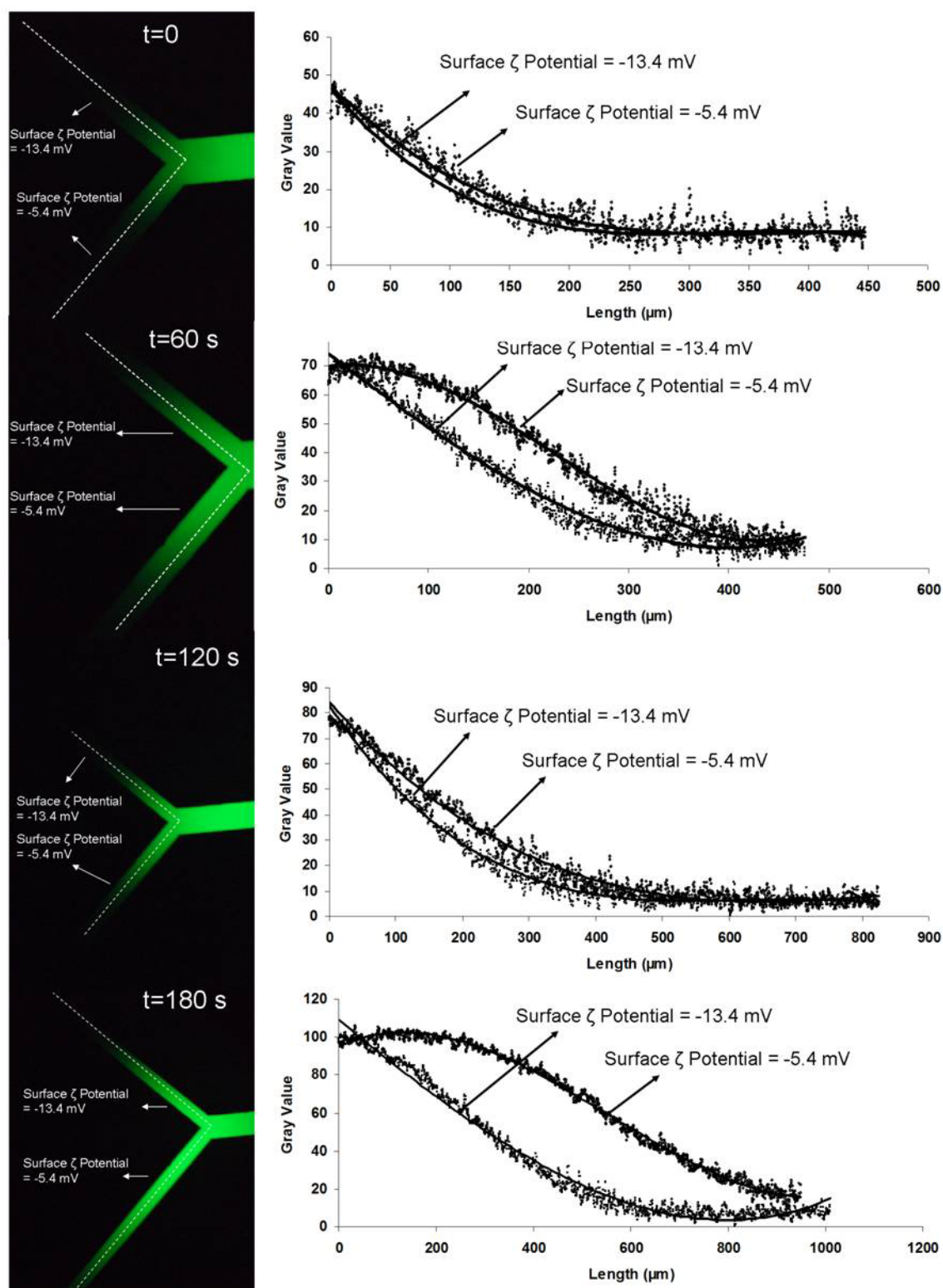
Figure 3.17: Flow directing images of the Fluorescein dye with intensity graphs along the center line in the channel

As presented in Table 3.8 the Fluorescein dye average intensity value ratios for the average intensity value in the native glass channel with -13.4 mV surface zeta potential channel, and in the surface modified channel with -5.4 mV surface zeta potential channel starts with 0.91 at t=0 and reach to 0.56 at t=400s. This suggests that at t=400s there is 1.79 times higher Fluorescein dye intensity in $-NH_2$ terminated channel compared to the Fluorescein dye intensity in native glass channel which is due to the higher electroosmotic flow rate of Fluorescein in the $-NH_2$ terminated channel. The higher electroosmotic flow rate of the Fluorescein dye in $-NH_2$ terminated channel is due to the higher surface zeta potential for the dye which relates to electroosmotic flow rate of the dye with equations (2) and (3).

Table 3.8: Average intensity values of the Fluorescein dye in channels

	Channel (-13.4 mV) Average Intensity (Gray Value)	Channel (-5.4 mV) Average Intensity (Gray Value)
Fluorescein (t=0 s)	14.91	16.36
Fluorescein (t=60 s)	20.10	24.31
Fluorescein (t=120 s)	27.99	38.27
Fluorescein (t=180 s)	36.34	65.39

The CFD results for the electrokinetic flow directing with altering the surface zeta potential is presented in Figure 3.17 and 3.18. The concentration values at center line along both channels are also presented in figures. It should be noted that CFD modeling does not encounter for charge of species.
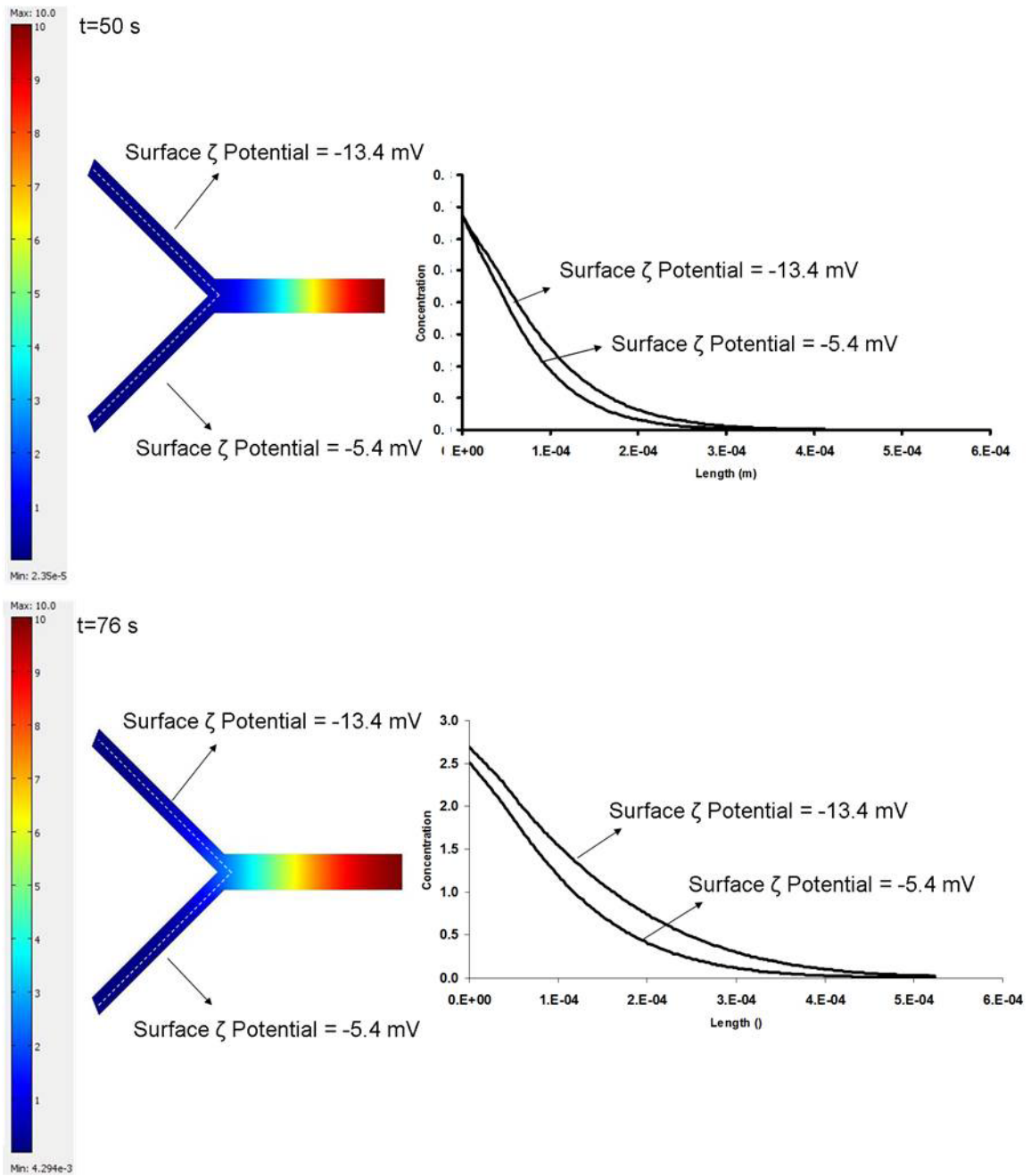
Figure 3.18: Flow directing with the CFD modeling of the device. Images and the concentration graphs of the mid line in the channel for t=0 and t=50s is presented in the image with dashed line
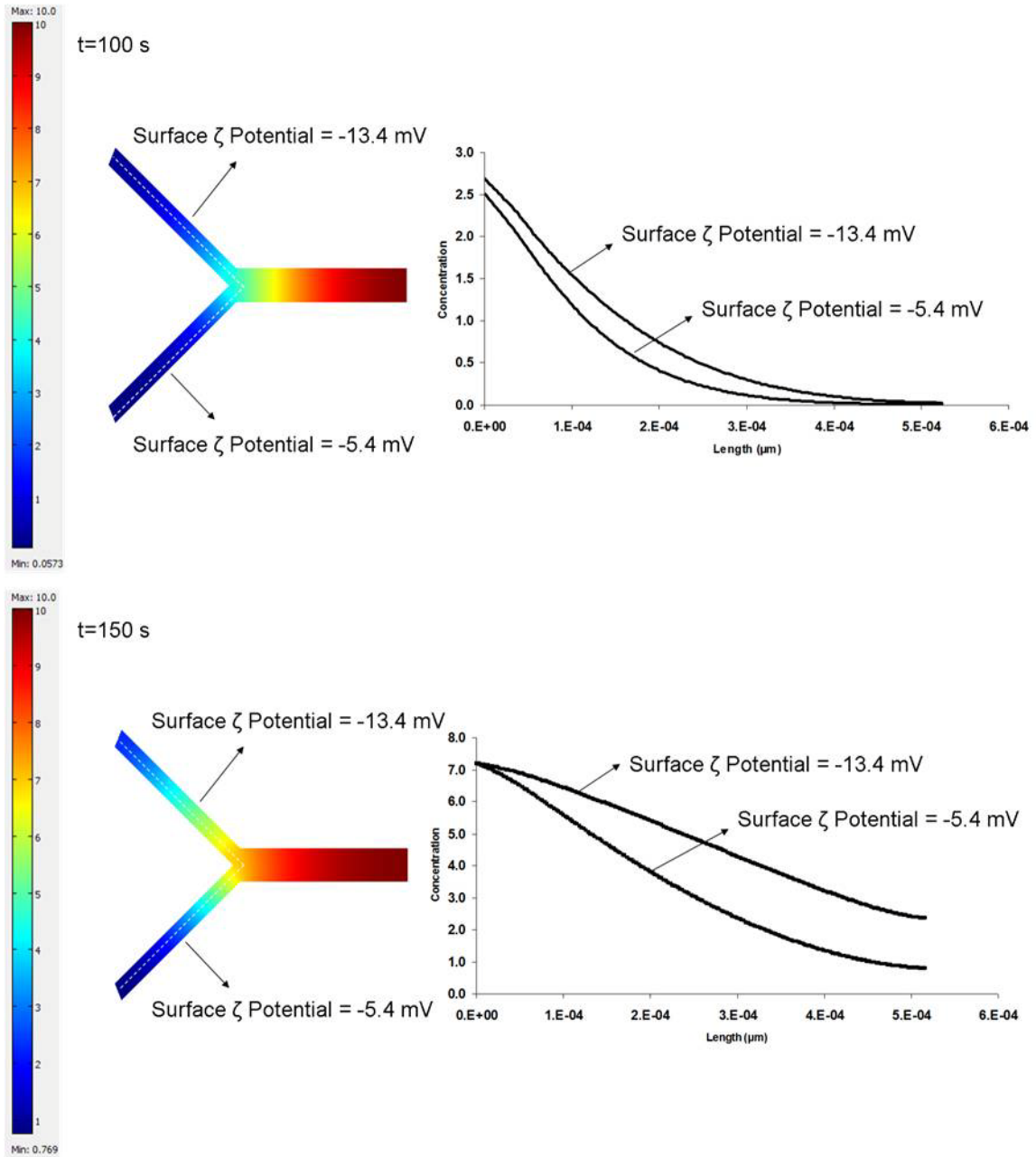
Figure 3.19: Flow directing with the CFD modeling of the device. Images and the concentration graphs of the mid line in the channel for t=0 and t=50s is presented in the image with dashed line

Table 3.9: Average concentration values in the channels

	Channel (-13.4 mV) Average Concentration (mM)	Channel (-5.4 mV) Average Concentration (mM)
CFD (t=50 s)	0.122	0.0992
CFD (t=76 s)	0.762	0.559
CFD (t=100 s)	1.783	1.282
CFD (t=150 s)	4.755	3.334

As presented in Table 3.10, concentration value ratios for the concentration values in the channel with -13.4 mV surface zeta potential, and in the channel with -5.4 mV surface zeta potential channel starts with 0.81 at t=0 and reach to 0.70 at t=150s. This suggests that at t=150s there is 1.43 times higher concentration in the channel with -13.4 mV surface zeta potential compared to the concentration in the channel with -5.4 mV surface zeta potential which is due to the higher electroosmotic flow rate in the channel with -13.4 mV surface zeta potential. The higher electroosmotic flow rate is due to the higher surface zeta potential for the dye which relates to electroosmotic flow rate of a substance with equations (2) and (3). The CFD simulations under predicts the directing ratio when compared to the experimental results. This is because of the 2D numerical simulation of the system.

Chapter 4

Conclusion and Future Work

4. Introduction

In this chapter conclusions of this work and some highlights of a few open questions leading to possible future work are discussed. In this thesis, stability of bromo, amino, and methyl-terminated surface layers against acid, base, solvent, oxidative plasma, thermal, and UV light exposures was evaluated. Chemically modified surfaces were investigated in microfluidic devices to show the importance of ζ potentials and surface charge. In addition, by tuning the surface charge density, ζ potential was also manipulated to show evidence of surface directed electroosmotic flow.

4.1 Conclusions

The summary of stability analysis of $-Br$, $-NH_2$ and $-CH_3$ terminated surface layers against a variety of common microfabrication and device operation conditions are presented in Table 4.1. It can be observed from Table 4.1 that of the 22 criteria evaluated the bromo surfaces are unstable to 5 conditions, the amino surfaces become unstable on exposure to 9 conditions, and the methyl terminated surfaces are the least stable with layer degradation observed under 11 conditions. Also it can be observed from Figure 3.9 that surfaces are stable to exposure of NaCl salt solution at 9 different pH conditions except 2 conditions for methyl terminated surfaces. It can be concluded that the methyl terminated surfaces become unstable for acids that is at pH 4 and less. Also, all three surfaces become unstable for oxidative plasma, HF acid, and piranha solution exposure conditions. Only the amine terminated surface become unstable against a basic solution exposure.

Table 4.1: Stability table for the surface adhered layers against exposure conditions

	−Br Terminated Surface	−NH₂ Terminated Surface	−CH₃ Terminated Surface
Exposure Condition	*Stability*	*Stability*	*Stability*
Cr Etchant	Stable	Stable	Unstable
Au Etchant	Stable	Stable	Unstable
HF	Unstable	Unstable	Unstable
Sulfuric Acid	Stable	Unstable	Unstable
HCl (32%)	Stable	Unstable	Unstable
Piranha Solution	Unstable	Unstable	Unstable
400K Developer	Stable	Stable	Stable
NaOH	Stable	Unstable	Stable
SC-1 Cleaning	Stable	Unstable	Unstable
Acetone	Stable	Stable	Stable
IPA	Stable	Stable	Stable
30 Watt	Unstable	Unstable	Unstable
50 Watt	Unstable	Unstable	Unstable
100 Watt	Unstable	Unstable	Unstable
90 ºC	Stable	Stable	Stable
150 ºC	Stable	Stable	Stable
205 ºC	Stable	Stable	Unstable
100 mJ/cm²	Stable	Stable	Stable
200 mJ/cm²	Stable	Stable	Stable
500 mJ/cm²	Stable	Stable	Stable
1000 mJ/cm²	Stable	Stable	Stable
1500 mJ/cm²	Stable	Stable	Stable

The surface directed flow was presented for both a positive and negatively charged dye, Rhodamine B and Fluorescein, respectively. From the data discussed in chapter 3, Rhodamine B intensity in the native glass surface channel with a -13.4 mV ζ potential is 1.92 times of the intensity in the surface modified channel with a -5.4 mV ζ potential. On the other hand Fluorescein intensity in the surface modified channel with a -5.4 mV ζ potential is 1.79 times higher in the native glass channel with a -13.4 mV ζ potential. These results indicate that even in microchannels influence of surface charge is tremendous and can extend beyond the few nm thick electric double layers. Therefore, surfaces can be used to direct flows in microchannels. In order to validate the experimental observation, CFD modeling was carried out by using existing theory. The CFD results show that the ratio between the modified and unmodified channels average concentration values along the center line is 0.7.

4.2 Future Work

The most important objective to be done in the future is to reach an 100% electrokinetic flow directing. CFD simulations predict that the 100% flow directing is possible for the channels with a surface ζ potential ratio of 10. But, as an experimental stand to fabricate such a high ζ potential difference between channels is challenging due to the need of different pH values and surface chemistries in channels.

Also, the inlet geometry of the channels, the number of inlet channels or the depth of the channels' effect on the electrokinetic flow directing by altering surface ζ potentials is not known.

Appendices

The methods for the fabrication of the chemically modified microfluidic device are discussed in chapter 2. The detailed description of the each procedure is presented in this part.

Appendix 1: Piranha Cleaning

1) Put H_2SO_4 and 30% diluted H_2O_2 to a clean glass beaker in the ratio of 4:1

2) Soak the sample holder boat in IPA

3) Clean the tweezer as following procedure

    a. Rinse with DI water

    b. Rinse with Acetone

    c. Rinse with IPA

    d. Rinse with DI water

    e. Rinse with IPA

    f. Dry under N_2 (Nitrogen) stream

4) Degrease glass slides as following procedure and place the slides in the boat

    a. Rinse with Acetone

    b. Rinse with IPA

    c. Rinse with DI water

    d. Rinse with IPA

5) Put DI water in a clean beaker

6) Take the boat with slides and soak into the DI water (Deionized Water).

7) Take the glass beaker with the boat and place it in an Ultrasound Cleaner for 5min

8) Take out the boat from the DI water and soak it in the piranha solution prepared before for 25 min at 60 ℃ – 65 ℃

9) To keep the piranha solution at the target temperature set the hot plate temperature to 190 ℃. Always monitor the solution temperature with a thermometer.

10) Take the warm solution and put it into an ultrasound cleaner for 5 min

11) Soak the boat with glass slides into the DI water for 1min

12) Rinse every glass slide with DI water while they are sitting in the boat

13) Soak the boat with glass slides into IPA (2-Propanol) for 1min

14) Take a plastic petri dish (Fischer Scientific), cut a cleanroom wipe and place the wipe in the petri dish

15) Degrease the tweezer

16) Take individual glass slide from boat

   a. Rinse with IPA

   b. Dry under N_2 stream

17) Place the cleaned glass slide in the petri dish on the cleanroom wipe

Appendix 2: Photomask with CAD Design
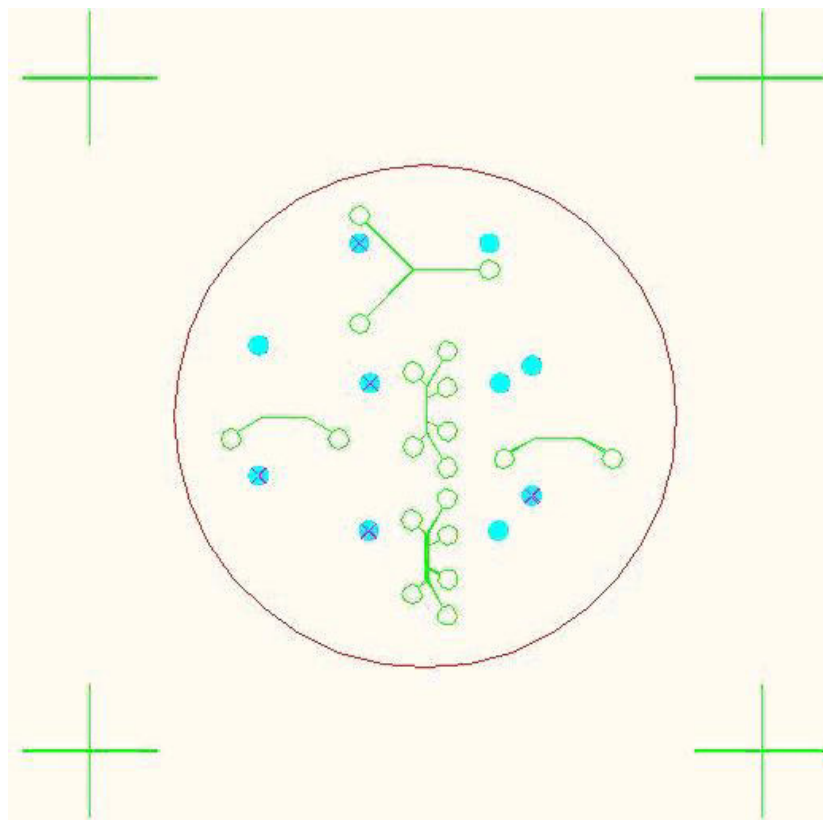
Figure A.1: Microfluidic device photomask CAD design
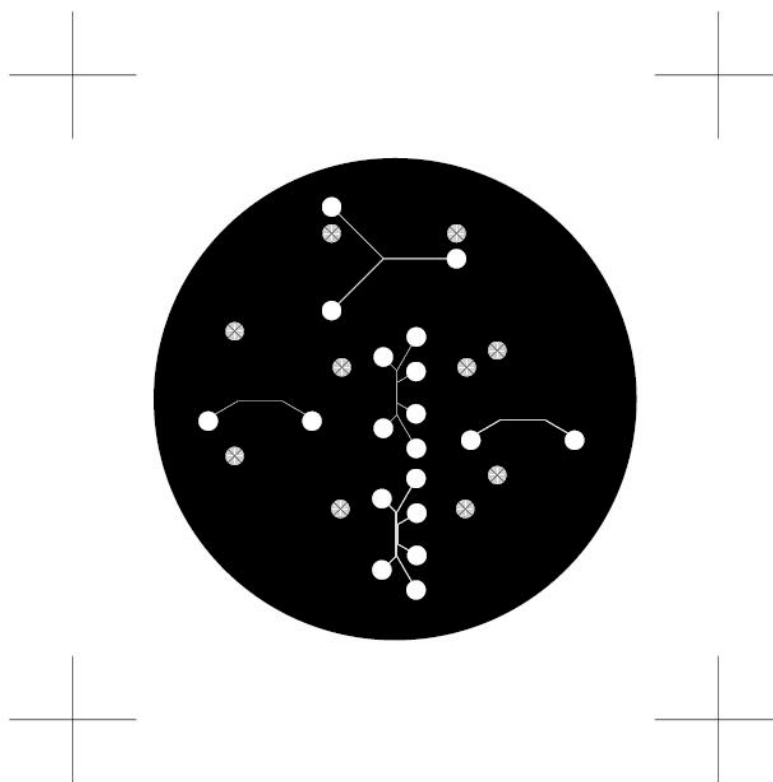
Figure A.2: Microfluidic device photomask

Appendix 3: Photolithography Procedure

1) Clean the tweezer

2) Degrease the photomask

3) Load the photomask in the mask aligner

4) Degrease the substrate

5) Prebake the substrate on hotplate at 150 ºC for 2 min

6) Place the substrate on a metal cooling block for 10 sec

7) Place the substrate on the spinner and spin coat the photoresist (AZ 1518) at 3000 rpm for 30 sec.

8) Softbake the substrate on a hotplate at 110 ºC for 3 min

9) Place the substrate on the mask aligner and align the "Y" model shape pattern on the photomask with the substrate and expose for 10 sec

10) Soak the substrate in the development solutions 4:1 DI water:AZ 400K and 10:1 DI water:AZ 400K for 90 sec and 30 sec respectively and agitate the solution gently during the process

11) Soak the substrate in the in DI water for 1 min and rinse with DI water

12) Dry the substrate under N_2 stream

13) Check the patterns on the substrate under microscope for any defects

14) Repeat steps 9-13 for modification side channels. Use alignment marks for patter alignment.

15) Hardbake the substrate at 110 ºC 30 sec

16) Soak the sample in Au etchant for 45 sec and agitate the solution gently

17) Soak the solution in DI water for 1 min and rinse the substrate with DI water

18) Dry the substrate under N_2 stream

19) Check the substrate for any defects under microscope

20) Soak the sample in Cr etchant for 30 sec and agitate the solution gently

21) Soak the solution in DI water for 1 min and rinse the substrate with DI water

22) Dry the substrate under N_2 stream

23) Check the substrate for any defects under microscope

24) Dry the substrate under N_2 stream

25) Soak the substrate in the diluted HF (4:1 DI Water:HF) for 10 min and agitate the solution gently

26) Soak the substrate in DI water for 1 min and rinse with DI water

27) Dry the substrate under N_2 stream

28) Degrease the substrate to strip the photoresist

29) Soak the substrate in the Au etchant for 10 min

30) Soak the substrate in DI water for 1 min and rinse with DI water

31) Dry the substrate under N_2 stream

32) Soak the substrate in the Cr etchant for 10 min

33) Soak the substrate in DI water for 1 min and rinse with DI water

34) Dry the substrate under N_2 stream

35) Soak the substrate in the diluted HF (4:1 DI Water:HF) for 10 min and agitate the solution gently

36) Soak the substrate in DI water for 1 min and rinse with DI water

37) Dry the substrate under N_2 stream

38) Degrease the substrate to strip the photoresist

39) Soak the substrate in the Au etchant for 10 min

40) Soak the substrate in DI water for 1 min and rinse with DI water

41) Dry the substrate under N_2 stream

42) Soak the substrate in the Cr etchant for 10 min

43) Soak the substrate in DI water for 1 min and rinse with DI water

44) Dry the substrate under N_2 stream

Appendix 4: Standard Cleaning 2 (SC-2)

1) Put H_2O, HCl, and 30% diluted H_2O_2 to a clean glass beaker in the ratio of 6:1:1

2) Soak the sample holder boat in IPA

3) Clean the tweezer

4) Degrease glass slides and place the slides in the boat

5) Put DI water in a clean beaker

6) Take the boat with slides and soak into the DI water (Deionized Water).

7) Take the glass beaker with the boat and place it in an Ultrasound Cleaner for 5min

8) Take out the boat from the DI water and soak it in the SC-2 cleaning solution prepared before for 25 min at 75 ℃ – 80 ℃

9) To keep the piranha solution at the target temperature set the hot plate temperature to 300 ℃. Always monitor the solution temperature with a thermometer.

10) Take the warm solution and put it into an ultrasound cleaner for 5 min

11) Soak the boat with glass slides into the DI water for 1min

12) Rinse every glass slide with DI water while they are sitting in the boat

13) Soak the boat with glass slides into IPA (2-Propanol) for 1min

14) Take a plastic petri dish, cut a cleanroom wipe and place the wipe in the petri dish

15) Clean the tweezer

16) Take individual glass slide from boat

    a. Rinse with IPA

    b. Dry under N_2 stream

17) Place the cleaned glass slide in the petri dish on the cleanroom wipe

Appendix 5: Glass Bonding

1) Prepare 1% Alconox solution in a glass vial

2) Prepare 0.5% Alconox 0.5% Calcium(II) Acetate Hydrate solution in a glass vial

3) Wipe the cover part with 1% Alconox solution for 2 min

4) Hold the cover slide and patterned slide together in one hand with a space between them

5) Rinse both slides with 0.5% Alconox 0.5% Calcium(II) Acetate Hydrate solution

6) Close slides together with trapping some 0.5% Alconox 0.5% Calcium(II) Acetate Hydrate solution between slides and move the top slide gently on the bottom slide to make the solution contact with all surface

7) Open slides apart and rinse slides with DI water not more than 30 sec

8) Close slides together with trapping some DI water between slides

9) Align holes on cover part to reservoirs on the patterned slide

10) Sandwich the device between two microscope slides

11) Fix slides together with paper clips

12) Bake at 60 ºC for an hour and check the bonding for any defects

13) Bake at 115 ºC for 2 hours

Appendix 6: Deposition of Br SAM

1) Start purging the glove bag with high purity N_2 (Airgas Inc, Radnor, PA)

2) Take 2 glass petri dishes from the oven and put them into the glove bag

3) Put 3 10ml new syringes and 2 1 ml new syringes to the glove bag

4) Put freshly cleaned (Piranha Cleaning) glass samples into the glove bag

5) Clean the tweezer and put it in to the glove bag

6) Zip the glove bag and leave an exhaust for continues N_2 flow

7) Purge the glove bag with N_2 to blow the glove bag and get the RH level under 2%

8) Lower N_2 flow to an amount that you can keep the RH level under the 2%

9) Take 10 ml anhydrous cyclohexane with 10 ml syringe

10) Inject the anhydrous cyclohexane to the functionalization glass dish

11) Take 0.1 ml 11-bromoundecyltrichlorosilane with 1ml syringe

12) Inject the 11-bromoundecyltrichlorosilane to the functionalization glass dish and agitate gently to mix the solution

13) Put glass samples to the in the functionalization solution in the functionalization dish

14) Cap the functionalization dish and leave samples in the functionalization solution for 2 hours

15) Take 10ml anhydrous cyclohexane and inject it to the rinsing dish

16) Take out samples from the functionalization solution

17) Soak samples in anhydrous cyclohexane in the rinsing dish for 2 min and agitate gently

18) Pour 15 ml DMF in another rinsing dish and put the dish in the glove bag

19) Transfer samples from anhydrous cyclohexane rinsing dish to the DMF rinsing dish

20) Carry the samples in the DMF rinsing dish to a ultrasound cleaner and sonicate for 2 minutes

21) Dry samples under N_2 stream and place them in the baking dish

22) Bake samples on a hotplate at 70 ºC under N_2

23) Put samples in a sterile plastic petri dish and store N_2 for future use if needed

Appendix 7: 'Click' modification of Br functionalized of surfaces

1) Prepare the azide solution:

    a. Put 15 ml of DMF in a scintillation vial

    b. Weigh and add 0.075 g of NaN_3 (sodium azide) to the scintillation vial, sonicate till all azide is dissolved. Keep bottle tightly capped and store in a secondary container away from metals and acids.

    c. Soak sample in saturated NaN_3/DMF solution for 48 hours

    d. Carefully remove sample from NaN_3/DMF bath. Rinse with DMF.

    e. Dry out sample under N_2 stream

2) Prepare a fresh 'click' solution

    a. Put 15 ml of ethanol In a scintillation vial

    b. Add 10 μl of propargylamine with a micro pipette to the vial

    c. Agitate gently to ensure complete dissolution

3) Prepare a fresh catalyst solution

    a. In a 50 ml clean volumetric flask put 50 ml DI water

    b. Add 12 mg copper sulphate pentahydrate ($CuSO_4 \cdot 5H_2O$)

    c. Add 20 mg sodium ascorbate

    d. Sonicate until all $CuSO_4 \cdot 5H_2O$ is dissolved

4) Mix the 'Click' solution and catalyst in a glass dish at the ratio of 5:1 (15ml Catalyst : 3ml propargylamine + ethanol Solution)

5) Soak samples in the solution for 2 hours

6) Clean the volumetric flask

    a. Get the beaker labeled as 0.1M HCl

    b. Put 50ml DI water

    c. Put 0.5ml HCl with 1ml pipette

    d. Pour the excess catalyst to the catalyst waste

    e. Pour the HCl solution to the volumetric flask and shake and pour the HCl solution to the HCl waste bottle

    f. Rinse the volumetric flask with DI water

7) Prepare 1% v/v NH_4OH

    a. Put 50ml DI water in a clean glass beaker

    b. Add 0.5ml NH_4OH with 1ml pipette

8) Remove sample carefully from the solution and rinse with ethanol and DI water

9) Place samples in a 1% v/v NH_4OH solution for 1 min

10) Take samples out and rinse with DI water followed by drying under N_2 stream

11) Store your samples in the sterile plastic petri dishes for future use

Appendix 8: Functionalization of microfluidic channels in microfluidic device with Br SAM

1) Align vacuum pump probe to one reservoir on the device

2) Start the pump fill other reservoirs with IPA

3) Wait until all channels are filled, and then take out IPA from the reservoirs with a Kimwipe and pump down the device to dry the channels

4) Turn off pump, carefully pull the device from the vacuum pump probe

5) Repeat steps 1-4 for DI water

6) Prepare the SC-1 cleaning solution

   a. Mix DI water: H_2O_2: NH_4OH at the ratio of 10:1:.1 (100mL DI: 10 mL H_2O_2: 1 mL NH_4OH) in a clean beaker

7) After DI water in channels are dried out take a small amount of the cleaning solution with pipette and put it in the reservoirs and wait till the channels are filled with SC-11 solution

8) Put cleaning solution on hot plate at 300^oC

9) Clean thermometer with acetone, IPA, DI water and put the thermometer in solution

10) Adjust the hot plate accordingly to maintain the 73^oC temperature

11) Once channels are filled with SC-1 solution stop the pump and put the device in hot solution for 10 minutes

12) Rinse the device with DI water, leave water in reservoirs except for top reservoir where the pump gets attached to that reservoir

13) Pump for 1 minute than take out DI water with a Kimwipe

14) Pump down to dry the channels

15) Fill reservoirs and channels with IPA and let them dry

16) Put device into a sterile petri dish, then bring it to the glove bag

17) Unplug pump and move set up to glove bag

18) Put the probe in the glove bag through the hole on top.

19) Tape around the hole once the probe is placed in

20) Start purging the glove bag with high purity N_2

21) Zip and lock the glove bag and leave an exhaust

22) Put a 1 mL syringe and two 10 mL syringe into the glove bag to be used for functionalization solution preparation

23) Lower the relative humidity less than 2%

24) Get a vial, and partially fill with DMF in the hood

25) Label vial DMF and put into the glove bag

26) Prepare fresh Br functionalization solution in a vial as a mixture of 10mL anhydrous cyclohexane and 0.1 ml of 11-bromoundecyltrichlorosilane in the glove bag

27) Add 10 ml of anhydrous cyclohexane into a vial in the glove bag

28) Turn on the pump and attach it to the device from the reservoir hole as specified in the schematic above

29) Put 1 drop of Br solution in the proper inlet which is shown in the schematic

30) Pump for 20 minutes with feeding the functionalization solution in the inlet one drop every 2 minutes

31) Take out the functionalization solution with a cleanroom wipe then put 1 drop of anhydrous cyclohexane in the inlet

32) Pump anhydrous cyclohexane for 10 minutes with feeding the anhydrous cyclohexane in the inlet every 2minutes

33) Take out the anhydrous cyclohexane from the reservoir with a cleanroom wipe and put a drop of DMF into the reservoir

34) Pump for 10 minutes with feeding DMF every 2 minutes

35) Take out the DMF with cleanroom wipe and pump down the channels to dry

36) Bake the device in the oven for 1 hour at 70^oC

Appendix 9: Functionalization of microfluidic channels in microfluidic device with – NH$_2$ group

1) Fill the microfluidic channels with saturated NaN$_3$/DMF solution with putting the solution to one inlet of the device with a glass pipette and vacuuming in an outlet with tweezer pump in the hood

2) Place the device in a sterile petri dish and close the cap. Let the device sit with saturated NaN$_3$/DMF solution in the microfluidic channels for 24 hours

3) Fill the device with DMF and flush channels for 2 minutes

4) Dry out reservoirs with Kimwipe and let the pump run to dry channels

5) Prepare the 'Click' functionalization solution for amine

6) Fill the microfluidic device with the 'Click' functionalization solution by pumping down form one outlet and introducing the functionalization solution from an inlet

7) Disconnect the pump and also put 'Click' functionalization solution to the reservoir which the pump was connected

8) Put the device in sterile plastic petri dish and let the device sit for 2 hours

9) Take out the 'Click' functionalization solution in reservoirs and dry channels with pump

10) Fill the channel with Ethanol and flush channels for 2 minutes

11) Take out the ethanol in reservoirs and dry the channels

12) Fill the channels with DI water and flush for 2minutes

13) Take out the DI water and dry channels.

14) Fill the channels with 1% v/v NH₄OH (Ammonium) solution and flush channels for 1

minute

15) Dry the channels and fill the channels with DI water following with flushing channels

for 2 minute with DI water

16) Dry the channels and put the device in sterile plastic petri dish for future use

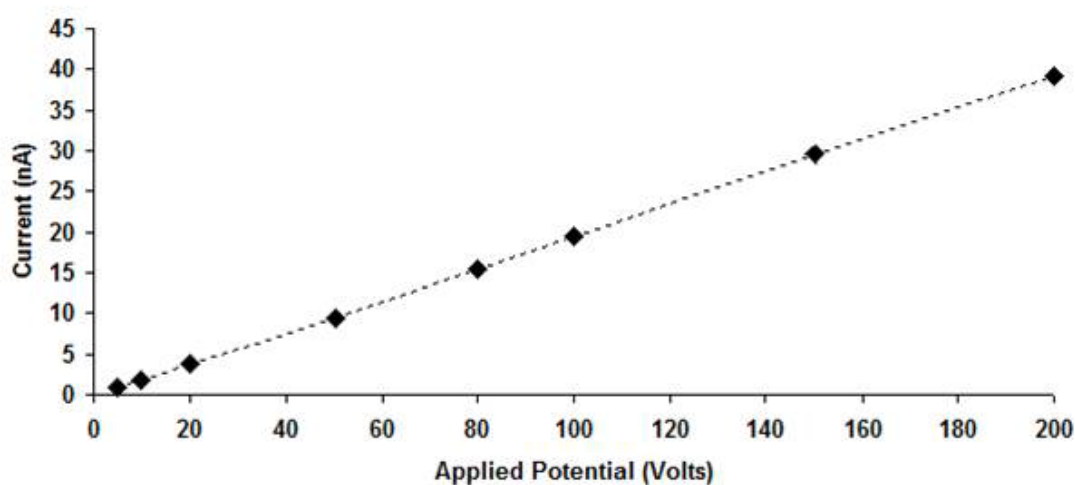**Appendix 10: I-V Measurements for Joule Heating Check**

Figure A.3: Applied potential measured current graph showing the Ohmic range for the microfluidic device

Bibliography

1. McDonald, J. C.; Duffy, D. C.; Anderson, J. R.; Chiu, D. T.; Wu, H.; Schueller, O. J. A.; Whitesides, G. M., Fabrication of Miocrofluidic Systems in poly(dimethylsiloxane). *Elecrophoresis* **2000,** 21, 27-40.
2. Prakash, S.; Piruska, A.; Gatimu, E. N.; Bohn, P. W.; Sweedler, J. V.; Shannon, M. A., Nanofluidics: Systems and Applications. *IEEE Sensors Journal* **2007,** 8.
3. Li, D., *Electrokinetics in Microfluidics*. Elsevier Academic Press: Toronto, 2004.
4. Terry, S. C.; Jerman, J. H.; Angell, J. B., A Gas Chromatographic Air Analyzer Fabricated on a Silicon Wafer. *IEEE Transactions On Electron Devices* **1979,** 26, 1880-1886.
5. Manz, A.; Miyahara, Y.; Miura, J.; Watanabe, Y.; Miyagi, H.; Sato, K., Design of an open-tubular column liquid chromatograph using silicon chip technology. Sensors and actuators. B, Chemical 1990, B1, 249-255.
6. Gravesen, P.; Branebjerg, J.; Jensen, O. S., Microfluidics-a review. *J. Micromech. Microeng.* **1993,** 3, 168-182.
7. Bassous, E.; Taub, H. H.; Kuhn, L., Ink jet printing nozzle arrays etched in silicon. *Applied Physics Letters* **1977,** 31, (2).
8. Whitesides, G. M., The origins and the future of microfluidics. *Nature* **2006,** 442, 368-373.
9. Ruska, W. E. A.; Carruth, G. F.; Kobayashi, R., Micropump-An Apparatus for Steady State Synthesis of Gas Mixtures at Very Dilute Concentrations. *The Review of Scientific Instruments* **1972,** 43, (9).
10. Zengerle, R.; Ulrich, J.; Kluge, S.; Richter, M.; Richter, A., A bidirectional silicon micropump. *Sensors and Actuators A* **1995,** 50, 81-86.
11. Reyes, D. R.; Iossifidis, D.; Auroux, P.-A.; Manz, A., Micro Total Analysis Systems. 1. Introduction, Theory, and Technology. *Anal. Chem.* **2002,** 74, 2623-2636.
12. Lemoff, A. V.; Lee, A. P., An AC magnetohydrodynamic micropump. *Sensors and Actuators B* **2000,** 63, 178-185.
13. Song, Y. J.; Zhao, T. S., Modelling and test of a thermally-driven phase-change nonmechanical micropump. *Journal of Micromechanics and Microengineering* **2001,** 11, 713-716.
14. Hatch, A.; Kamholz, A. E.; Holman, G.; Yager, P.; Bohringer, K. F., A Ferrofluidic Magnetic Micropump. *Journal of Microelectromechanical Systems* **2001,** 10, 215-221.
15. Choi, J.-W.; *al, e.*, Development and Characterization of Microfluidic Devices and Systems for Magnetic Bead-Based Biochemical Detection. *Biomed Microdevices* **2001,** 3, 191-200.
16. Oh, K. W.; Rong, R.; Ahn, C. H., Miniaturization of pinch-type valves and pumps for practical micro total analysis system integration. *J. Micromech. Microeng.* **2005,** 15, 2449-2455.
17. Rogge, T.; Rummler, Z.; Schomburg, W. K., Polymer micro valve with a hydraulic piezo-drive fabricated by the AMANDA process. *Sensors and Actuators A* **2004,** 110, 206-212.
18. Shao, P.; Rummler, Z.; Schomburg, W. K., Polymer micro piezo valve with a small dead volume. *J. Micromech. Microeng.* **2004,** 14, 305-309.

19. Zhang, C.; Xing, D.; Li, Y., Micropumps, microvalves, and micromixers within PCR microfluidic chips: Advances and trends. *Biotechnology Advances* **2007,** 25, (483-514).

20. Baechi, D.; Buser, R.; Dual, J., High-Density Microvalve Arrays for SampleProcessingin PCR Chips. *Biomed Microdevices* **2001,** 3, 183-190.

21. Vyawahare, S.; Sitaula, S.; Martin, S.; Adalian, D.; Scherer, A., Electronic control of elastomeric microfluidic circuits with shape memory actuators. *Lab On A Chip* **2008,** 8, 1530-1535.

22. Grover, W. H.; Skelley, A. M.; Liu, C. N.; Lagally, E. T.; Mathies, R. A., Monolithic membrane valves and diaphragm pumps for practical large-scale integration into glass microfluidic devices. *Sensors and Actuators B* **2003,** 89, 315-323.

23. Wego, A.; Richter, S.; Pagel, L., Fluidic microsystems based on printed circuit board technology. *J. Micromech. Microeng.* **2001,** 11, 528-531.

24. Suzuki, H.; Yoneyama, R., Integrated microfluidic system with electrochemically actuated on-chip pumps and valves. *Sensors and Actuators B* **2003,** 96, 38-45.

25. Liu, R. H.; Yu, Q.; Beebe, D. J., Fabrication and Characterization of Hydrogel-Based Microvalves. *Journal of Microelectromechanical Systems* **2002,** 11, (1), 45-53.

26. Wang, J.; Chen, Z.; Mauk, M.; Hong, K.-S.; Li, M.; Yang, S.; Bau, H. H., Self-Actuated, Thermo-Responsive Hydrogel Valves for Lab on a Chip. *Biomedical Microdevices* **2005,** 7, 313-322.

27. Liu, Y.; Rauch, C. B.; Stevens, R. L.; Lenigk, R.; Yang, J.; Rhine, D. B.; Grodzinski, P., DNA Amplification and Hybridization Assays in Integrated Plastic Monolithic Devices. *Anal. Chem.* **2002,** 74, 3063-3070.

28. Yamada, M.; Seki, M., Nanoliter-Sized Liquid Dispenser Array for Multiple Biochemical Analysis in Microfluidic Devices. *Anal. Chem.* **2004,** 76, 895-899.

29. Ahn, C. H.; Choi, J.-W.; Beaucage, G.; Nevin, J. H.; Lee, J.-B.; Puntambekar, A.; Lee, J. Y., Disposable Smart Lab on a Chip for Point-of-Care Clinical Diagnostics. *PROCEEDINGS OF THE IEEE* **2004,** 92, 154-173.

30. Andersson, H.; Wijngaart, W. v. d.; Griss, P.; Niklaus, F.; Stemme, G., Hydrophobic valves of plasma deposited octafluorocyclobutane in DRIE channels. *Sensors and Actuators B* **2001,** 75, 136-141.

31. Prakash, S.; Karacor, M. B.; Banerjee, S., Surface modification in microsystems and nanosystems. *Surface Science Reports* **2009,** Article In Press.

32. Reuss, F. F., *Natural* **1809,** 2, (327).

33. Leea, J. S. H.; Renb, C. L.; Li, D., Effects of surface heterogeneity on flow circulation in electroosmotic flow in microchannels. *Analytica Chimica Acta* **2005,** 530, 273-282.

34. Biddiss, E.; Erickson, D.; Li, D., Heterogeneous Surface Charge Enhanced Micromixing for Electrokinetic Flows. *Anal. Chem.* **2004,** 76, 3208-3213.

35. Stroock, A. D.; Weck, M.; Chiu, D. T.; Huck, W. T. S.; Kenis, P. J. A.; Ismagilov, R. F.; Whitesides, G. M., Patterning Electro-osmotic Flow with Patterned Surface Charge. *Physical Review Letters* **2000,** 84.

36. Zhang, P.; Qiu, H. H., Investigation of the patterned surface modification on 3D vortex flow generation in a micropipe. *J. Micromech. Microeng.* **2008,** 18, 115030.

37. Herr, A. E.; Molho, J. I.; Santiago, J. G.; Mungal, M. G.; Kenny, T. W.; M. G, G., Electroosmotic Capillary Flow with Nonuniform Zeta Potential. *Anal. Chem.* **2000,**

72, 1053-1057.

38. Prakash, S.; Long, T. M.; Selby, J. C.; Moore, J. S.; Shannon, M. A., "Click" Modification of Silica Surfaces and Glass Microfluidic Channels. *Anal. Chem.* **2007,** 79, 1661-1667.

39. Salim, M.; Wright, P. C.; McArthur, S. L., Studies of electroosmotic flow and the effects of protein adsorption in plasmapolymerized microchannel surfaces. *Elecrophoresis* **2009,** 30, 1877-1887.

40. Vourdas, N.; Tserepi, A.; Boudouvis, A. G.; Gogolides, E., Plasma processing for polymeric microfluidics fabrication and surface modification: Effect of super-hydrophobic walls on electroosmotic flow. *Microelectronic Engineering* **2008,** 85, 1124-1127.

41. Krishnamoorthy, S.; Feng, J.; Henry, A. C.; Locascio, L. E.; Hickman, J. J.; Sundaram, S., Simulation and experimental characterization of electroosmotic flow in surface modified channels. *Microfluid Nanofluid* **2006,** 2, 345-355.

42. Stein, D.; Kruithof, M.; Dekker, C., Surface-Charge-Governed Ion Transport in Nanofluidic Channels. *Physical Review Letters* **2004,** 93, (3).

43. Zhao, B.; Moore, J. S.; Beebe, D. J., Surface-Directed Liquid Flow Inside Microchannels. *Science* **2001,** 291.

44. Cox, J. D.; Curry, M. S.; Skirboll, S. K.; Gourley, P. L.; Sasaki, D. Y., Surface passivation of a microfluidic device to glial cell adhesion: a comparison of hydrophobic and hydrophilic SAM coatings. *Biomaterials* **2002,** 23, 929–935.

45. Ulman, A., Formation and Structure of Self-Assembled Monolayers. *Chem. Rev.* **1996,** 96, 1533-1554.

46. Schreiber, F., Structure and Growth of self-assembling monolayers. *Progress in Surface Science* **2000,** 65, 151-256.

47. T. Vallant, J. K., H. Brunner, U Mayer, H. Hoffmann, Investigation of the Formation and Structure of Self-assembled Alkylsiloxane Monolayers on Silicon Using In Situ Attenuated Total Reflection Infrared Spectroscopy. *Langmuir* **1999,** 1999, (15).

48. J. B. Brzoska, I. B. A., F. Rondelez, Silanization of Solid Substrates: A Step toward Reproducibility. *Langmuir* **1994,** 10, 4367-4373.

49. Reena Banga, J. Y., Anthony M. Morgan, Brian Evans, Jaqueline Kells, FTIR and AFM Studies of the Kinetics and Self-Assembly of Alkyltrichlorosilanes onto Glass and Silicon. *Langmuir* **1995,** 11, 4393-4399.

50. I. M. Tidswell, B. M. O., P. S. Pershan, S. R. Wasserman, G. M. Whitesides, J. D. Axe, X-ray specular reflection studies of silicon coated by organic monolayers (alkylsiloxanes). *The American Physical Society* **1990,** 41, 1111-1127.

51. N. Balachander, C. N. S., Monolayer Transformation by Nucleophilic Substitution: Applications to the Creation of New Monolayer Assemblies. *Langmuir* **1990,** 6, 1621-1627.

52. P. Silberzan, L. L., D. Ausserre, J. J. Benattar, Silanation of Silica Surfaces. A New Method of Constructing Pure or Mixed Monolayers. *Langmuir* **1991,** 7, (8), 1647-1651.

53. Stephen R. Wasserman, Y.-T. T., and George M. Whitesides, Structure and Reactivity of Alkylsiloxane Monolayers Formed by Reaction of Alkyltrichlorosilanes on Silicon Substrates. *Langmuir* **1989,** 5, (4), 1074-1087.

54. Atul N. Parikh, D. L. A., Issam Ben Azouz, Francis Rondelez, An Intrinsic

Relationship between Molecular Structure in Self-Assembled n-Alkylsiloxane Monolayers and Deposition Temperature. *J. Phys. Chem* **1994,** 98, 7577-7590.

55. Sidney R. Cohen, R. N., and Jacob Sagiv, Thermally Induced Disorder in Organized Organic Monolayes on Solid Substrates. *J. Phys. Chem* **1986,** 90, 3054-3056.

56. A. G. Richter, M. K. D., C. J. Yu, P. Dutta, In Situ Time-Resolved X-ray Reflectivity Study of Self-Assembly from Solution. *Langmuir* **1998,** 14, 5980-5983.

57. H. Brunner, T. V., U. Mayer, H. Hoffmann, Substrate Effects on the formation of Alkylsiloxane Monolayers. *Langmuir* **1999,** 15, 1899-1901.

58. T. Vallant, H. B., U. Mayer, H. Hoffmann, T. Leitner, R. Resch, G. Friedbacher, Formation of Self-Assembled Octadecylsiloxane Monolayers on Mica and Silicon Surfaces Studied by Atomic Force Microscopy and Infrared Spectroscopy. *J. Phys. Chem B* **1998,** 102, (7190-7197).

59. T. Komeda, K. N., Y. Nishioka, Octadecyltrichlorosilane self-assembled-monolayer islands as a self-patterned-mask for HF etching of SiO2 on Si. *J. Vac. Sci. Technol.* **1998,** A 16, 1680-1685.

60. Kolb, H. C.; Finn, M. G.; Sharpless, K. B., Click Chemistry: Diverse Chemical Function from a Few Good Reactions. *Angewandte Chemie* **2001,** 40, (11), 2004-2021.

61. Shaurya Prakash, T. M. L., John C. Selby, Jeffrey S. Moore, Mark A. Shannon, "Click" Modification of Silica Surfaces and Glass Microfluidic Channels. *Anal. Chem.* **2007,** 79, 1661-1667.

62. Claudia Haensch, S. H., Ulrich S Schubert, Chemical surface reactions by click chemistry: coumarin dye modification of 11-bromoundecyltrichlorosilane monolayers. *Nanotechnology* **2008,** 19.

63. Allen, P. B.; Chiu, D. T., Calcium-Assisted Glass-to-Glass Bonding for Fabrication of Glass Microfluidic Devices. *Anal. Chem.* **2008,** 80, 7153-7157.

64. Wu, Y.; Karacor, M. B.; Prakash, S.; Shannon, M. A., Characterization of the Solid/Water Interface of Functionalized Silica Surfaces by Atomic Force Microscopy *Submitted*.